IOP Publishing | Journal of Physics D: Applied Physics
J. Phys. D: Appl. Phys. **40** (2007) R249–R271 doi:10.1088/0022-3727/40/14/R01

TOPICAL REVIEW

Ultrafast nonlinear all-optical processes in silicon-on-insulator waveguides

R Dekker[1], **N Usechak**[2], **M Först**[3] **and A Driessen**[1]

[1] Integrated Optical Micro Systems, MESA+, University of Twente, PO Box 217, 7500 AE Enschede, The Netherlands
[2] Trumpf Photonics Inc., 2601 US Route 130 South, Cranbury, NJ 08512, USA
[3] RWTH Aachen University, Institut für Halbleitertechnik, 52074 Aachen, Germany.

E-mail: r.dekker@utwente.nl

Received 3 April 2007, in final form 14 May 2007
Published 29 June 2007
Online at stacks.iop.org/JPhysD/40/R249

Abstract
In this review we present an overview of the progress made in recent years in the field of integrated silicon-on-insulator (SOI) waveguide photonics with a strong emphasis on third-order nonlinear optical processes. Although the focus is on simple waveguide structures the utilization of complex structures such as microring resonators and photonic crystal structures is briefly discussed as well. Several fabrication methods are explained and methods which improve optical loss, coupling efficiency and polarization dependence are presented.

As the demand for bandwidth increases communication systems are forced to use higher bit rates to accommodate the load. A consequence of high-bit-rate systems is that they require short pulses where the importance of waveguide dispersion tailoring becomes increasingly important. The impact of short pulses on the efficiency of all-optical processes is discussed and recent accomplishments in this field are presented. Numerical results of femtosecond, picosecond and nanosecond pulse propagation in SOI waveguides are compared to provide an insight into the physical processes that dominate at these different time scales. In this work we focus on two-photon absorption (TPA), free-carrier absorption (FCA), plasma dispersion and the optical Kerr effect. After describing these nonlinear effects, some other important all-optical processes based on plasma dispersion and the Kerr effect are described, namely cross-absorption modulation (XAM), self-phase modulation (SPM), cross-phase modulation (XPM), four-wave mixing (FWM) and stimulated Raman scattering (SRS). The latter provides the best hope for practical and/or commercial applications and finds its use in amplification and lasing. Furthermore, we present some guidelines for efficient numerical modelling of propagation in SOI waveguides.

This review is a good starting point for those who are new in this hot and rapidly emerging field and gives an overview of important considerations that need to be taken into account when designing, fabricating and characterizing SOI waveguides for ultrafast third-order nonlinear all-optical processing.

0022-3727/07/140249+23$30.00 © 2007 IOP Publishing Ltd Printed in the UK

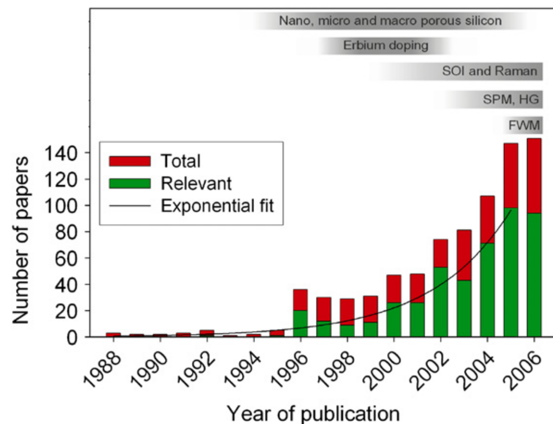

Figure 1. Web of Science literature search on SOI. Search condition: TI = (silicon* AND waveguide*) OR TI = (silicon* AND resonator*) OR TI = (silicon* AND photonic*). Only part of the total search results yielded topics that were relevant with respect to integrated optics. The data for 2006 only includes the months January through October.

(This figure is in colour only in the electronic version)

1. Introduction

Because of its potential for integration with microelectronics [1] silicon photonics is receiving considerable attention. This is in large part due to the fact that optical systems can provide more bandwidth for data transport and switching than any electronic approach. Figure 1 shows the results of a literature search on the Web of Science [2], which was conducted on article titles with the words 'silicon AND waveguide', or 'silicon AND resonator', or 'silicon AND photonic' in the period from 1988 till October 2006. The bottom bars indicate the number of papers per year that turned out to be relevant with respect to silicon integrated optics. Although this graph does not represent all papers on silicon photonics, it is clear that there is an exponential trend in the number of publications on this topic; a clear indication of its popularity and future potential. Furthermore, the shaded areas above the bar chart give an indication about the main contents of the papers. For instance, it shows that several groups were working on doping silicon with erbium for light emission purposes between 1996 and 2000. In the period from 2000 till 2004 a shift from porous silicon to single crystalline SOI took place. From that moment, Raman gain was studied by many groups and nonlinear processes such as SPM and FWM became topics of particular interest.

Several review papers have already been published on SOI photonics, focusing on the recent accomplishments of light emission at telecommunication wavelengths [3, 4], modulation using p-i-n structures and free-carrier injection [3–6], and linear and nonlinear optical processes in SOI photonic devices [7]. For example, Soref recently presented an overview of the past, present and future prospects of silicon photonics [8]. However, most of these papers discuss results on a broad range of device geometries and material varieties (erbium doping, P and N doping, Si–Ge, etc) for the emission and detection of light in silicon optical waveguides. The fact that silicon is an indirect bandgap material imposes physical limitations with respect to light emission and detection in the infrared. This is a serious drawback when compared with integrated optical devices based on III-V direct bandgap materials which are capable of efficiently emitting and detecting light. Overcoming this limitation in silicon is considered to be the holy grail of silicon photonics. Besides the work on light emitting silicon [3, 4, 9], considerable effort has been put into engineering silicon-based devices that are capable of enhanced light detection in the near infrared, such as laser assisted surface texturing [10], proton [11] and Si-ion implantation [12], the integration of germanium on pure silicon [13] and germanium on silicon p-i-n photodiodes [14] and monolithically integrated Si–Ge heterojunction photodetectors [15].

The development of active functions like emission and detection of light in silicon waveguides is extremely important for the future success of silicon nanophotonics. In addition, all-optical processes are of similar importance, since these typically high-speed processes offer the possibility to overcome the physical speed limitations of today's electronics.

The aim of this paper is to present the third-order nonlinear optical properties of silicon optical waveguides and the methods needed to influence and optimize these properties for applications in next generation high-speed all-optical devices. In recent years many types of nonlinear optical phenomena have been investigated in silicon-based nanophotonic devices. Substantial progress has been achieved, e.g. in the field of Raman amplification, in both continuous-wave [16] and pulsed pump–probe [17, 18] experiments. Further, nonlinear effects such as two-photon absorption (TPA) [19], self-phase modulation (SPM) [20–22], cross-phase modulation (XPM) [23], continuum generation [24], four-wave mixing (FWM) [25] and the optical Kerr effect [26] have also been successfully demonstrated and thoroughly investigated, on time scales ranging from the femtosecond to the nanosecond regime.

Aside from these nonlinear optical effects, which are well known in the field of fibre optics, an increasing number of exotic experiments and discussions are emerging within the field of SOI photonics as time scales decrease and local optical field densities increase. Despite the fact that these non-conventional phenomena are beyond the scope of this manuscript, they are worth mentioning. Some examples of such recent accomplishments are the generation of quasi particles in silicon using ultrashort (10 fs) laser pulses [27] and broadband, high-efficiency, opto-mechanical, wavelength conversion in photonic crystal devices exploiting the radiation pressure of the optical field [28]. Furthermore, the generation of correlated photons within a CMOS-compatible silicon waveguide [29] opens the way to scaleable quantum information processing devices.

As mentioned earlier, the scope of this review paper is to present the third-order nonlinear all-optical processes that can be exploited in SOI waveguides for high-speed optical processing of data. Therefore, after a review of the nonlinear processes in section 2, two efficient modelling methods are presented in section 3 that give a good insight into the propagation of short light pulses, the carrier dynamics, and the nonlinear processes in straight SOI waveguides.

Thereafter, in section 4, various methods are listed to tailor the waveguide properties, such that the propagation losses, the optical coupling, dispersion, polarization and field intensities can be optimized. All these properties are of major importance for efficient all-optical switching.

Finally, some general conclusions are listed in section 5.

2. Nonlinear processes in silicon

The polarization P of a medium through which optical signals with frequency ω are propagating can be expressed in a power series with respect to the applied electric field E_ω in the frequency domain:

$$P = \varepsilon_0[\chi^{(1)}E_\omega + \chi^{(2)}E_\omega E_\omega + \chi^{(3)}E_\omega E_\omega E_\omega + \cdots], \quad (1)$$

where ε_0 is the permittivity of free space (8.85×10^{-12} F m^{-1}) and $\chi^{(i)}$ is the ith order susceptibility tensor of the medium. The first-order tensor is responsible for the linear optical properties, whereas the higher-order terms contribute to nonlinear effects. In nonlinear optics the nonlinear interaction between the laser field and the medium is studied. Since a CW laser field typically has one or more monochromatic Fourier components, the field-induced nonlinear polarization can also be composed of a number of Fourier components where, according to equation (1), the linear component is given by

$$P^{(1)}(\omega) = \varepsilon_0\chi^{(1)}(\omega)E_\omega. \quad (2)$$

Similarly the second-order nonlinear polarization can be written as

$$P^{(2)}(\omega) = \varepsilon_0\chi^{(2)}(\omega; \omega_1, \omega_2)E_{\omega_1}E_{\omega_2}. \quad (3)$$

The nonlinear susceptibility $\chi^{(2)}$ is a third-order tensor with $3\times 9 = 27$ elements and is responsible for the electro-optic effect. In principle, silicon does not exhibit a linear electro-optic (Pockels) effect due to its centro-symmetric crystal structure [30]. However, we should point out that a significant linear electro-optic effect has recently been induced in silicon by breaking the crystal symmetry through deposition of a straining layer on top of a silicon waveguide, resulting in an induced second-order nonlinear coefficient $\chi^{(2)}$ of $\approx$15 pm V^{-1} [31]. Materials with a high $\chi^{(2)}$ value can be used for sum- and difference-frequency generation and frequency doubling. In sum-frequency (difference-frequency) generation, light with a new frequency $\omega = \omega_1 + \omega_2$ ($\omega = \omega_1 - \omega_2$) can be generated by two incident monochromatic waves having frequencies ω_1 and ω_2. Since the focus of this paper is on the nonlinear effects of un-strained silicon, $\chi^{(2)}$ is negligibly small and these effects are not observed with any strength.

However, the third-order nonlinear polarization, which takes the form

$$P^{(3)}(\omega) = \varepsilon_0 K\chi^{(3)}(-\omega; \omega_1, \omega_2, \omega_2)E_{\omega_1}E_{\omega_2}E_{\omega_3}, \quad (4)$$

where K is a constant that depends on the particular optical process is not negligible in silicon [7]. In equation (4) $\chi^{(3)}$ is a fourth-order tensor comprising $3 \times 27 = 81$ elements. In the special case where the input is monochromatic two third-order nonlinear polarizations are obtained [7]:

$$P^{(3)}(\omega) = \varepsilon_0\frac{3}{4}\chi^{(3)}(-\omega; \omega, -\omega, \omega)|E_\omega|^2E_\omega, \quad (5)$$

$$P^{(3)}(3\omega) = \varepsilon_0\frac{1}{4}\chi^{(3)}(-3\omega; \omega, \omega, \omega)E_\omega^3. \quad (6)$$

Equation (5), which is discussed in sections 2.1 and 2.3 in greater detail, describes both the degenerate TPA and the optical Kerr effect which are related to the imaginary and real parts of $\chi^{(3)}$, respectively. Equation (6) represents third-harmonic generation, which can be neglected when working at telecommunication wavelengths, since the third-harmonic green light that will be generated from signals with a wavelength around 1500 nm is absorbed strongly by the silicon.

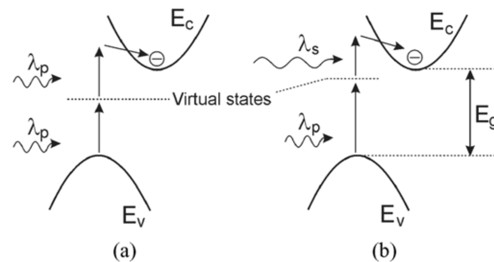

Figure 2. Schematic representation of TPA in silicon. (*a*) Degenerate. (*b*) Non-degenerate.

2.1. Two-photon absorption

Two-photon absorption is of particular relevance when dealing with high intensity infrared light propagation in silicon waveguides. Figure 2 shows a schematic representation of the TPA process in silicon. When the total energy of two photons is larger than the bandgap energy of the silicon ($E_g = E_c - E_v$), they can both be absorbed exciting an electron from the valence band (upper energy E_v) to the conduction band (lower energy E_c), producing an electron-hole pair. We can distinguish between two types of TPA, i.e. a degenerate and a non-degenerate process. In degenerate TPA, two photons with the same wavelength are absorbed by means of a phonon-assisted process. For instance this is the case when strong pump lasers are used with a pump wavelength λ_p (see figure 2, left). As a result the pump power will be depleted along the waveguide [32].

In non-degenerate TPA, one photon with wavelength λ_p from a pump source and one photon from a signal source with wavelength λ_s are both absorbed by means of a photon-assisted non-degenerate process [33]. Typically, $\lambda_s > \lambda_p$ in pump–probe experiments. This means that a signal photon is only absorbed when a pump photon is present (see figure 2, right). This phenomenon can be employed for cross-amplitude modulation (XAM) [32] and is discussed in section 2.2 in further detail.

The number of free carriers N in a silicon waveguide subjected to a time-varying optical intensity is governed by the free-carrier generation and recombination rates according to

$$\frac{dN(t)}{dt} = \frac{\beta}{2hv}I^2(t) - \frac{N(t)}{\tau}. \quad (7)$$

Here, $dN(t)/dt$ is the temporal change of the free-carrier density. Of course when a continuous-wave (CW) light source is used, equation (7) reduces to [34, 35]:

$$N = \frac{\beta I^2\tau}{2hv}. \quad (8)$$

The first term at the right-hand side of equation (7) describes the generation of free carriers, where hv is the energy of a single

photon, I is the intensity of the field in W m^{-2} and β is the TPA coefficient which ranges from 5×10^{-12} to 9×10^{-12} m W^{-1} [17,26,36–38]. The latter is related to the imaginary part of $\chi^{(3)}$ via

$$\beta = \frac{3\pi \chi^{(3)}_{Im}}{c\varepsilon_0 \lambda n_0^2}. \tag{9}$$

Moreover, c is the speed of light, λ is the wavelength of the light and n_0 is the linear refractive index of the material. TPA will induce a linear intensity dependence on the total absorption of the medium:

$$\alpha(I) = \alpha + \beta I, \tag{10}$$

where α is a linear absorption coefficient. The second term on the right-hand side of equation (7) is responsible for a decrease in the free-carrier density by means of electron–hole pair recombination. The recombination lifetime τ is on the order of 100 ns for bulk silicon but depends strongly on the geometry particularly when dealing with submicrometre sized planar waveguides [37], therefore reported values range from picoseconds to 200 ns. The free-carrier lifetime limits the switching or modulation speed of devices based on free-carrier injection; some methods used to decrease the recombination time will be discussed in section 4.2. The absorption of photons causes depletion of the signal along the waveguide, which can be described by

$$\frac{\mathrm{d}I}{\mathrm{d}z} = \beta I^2. \tag{11}$$

Free carriers will be generated as a result of TPA in silicon due to the excitation of electrons from the valence band to the conduction band. The generated holes and electrons give rise to FCA and are responsible for the plasma dispersion effect, which is described in the next subsection. The losses caused by TPA and FCA prove to be a serious limitation that can severely degrade the performance of ultrafast all-optical devices that are based on the optical Kerr effect [39].

2.2. *Free-carrier dispersion*

The plasma dispersion effect is related to the free-carrier density in a semiconductor and changes both the real and the imaginary part of the refractive index, $n_0 = n + \mathrm{i}k$, respectively. The imaginary part of the refractive index is related to the linear absorption α via

$$\alpha = \frac{4\pi k}{\lambda}. \tag{12}$$

The changes in the complex refractive index are governed by the Drude–Lorenz equations that describe how the electron and hole concentrations (N_e and N_h expressed in cm^{-3}) influence the absorption α and the real part of the refractive index n:

$$\Delta\alpha = -\frac{e^3\lambda^2}{4\pi^2 c^3 \varepsilon_0 n}\left[\frac{\Delta N_\mathrm{e}}{m_\mathrm{ce}^2 \mu_\mathrm{e}} + \frac{\Delta N_\mathrm{h}}{m_\mathrm{ch}^2 \mu_\mathrm{h}}\right], \tag{13}$$

$$\Delta n = -\frac{e^2\lambda^2}{8\pi^2 c^2 \varepsilon_0 n}\left[\frac{\Delta N_\mathrm{e}}{m_\mathrm{ce}} + \frac{\Delta N_\mathrm{h}}{m_\mathrm{ch}}\right]. \tag{14}$$

Here e is the electron charge, n the refractive index of unperturbed crystalline silicon, m_ce and m_ch are the conductivity effective masses and μ_e and μ_h the mobility of electrons and holes, respectively. For silicon, the conductivity effective masses are $m_\mathrm{ce} = 0.26m_0$ and $m_\mathrm{ch} = 0.39m_0$, with m_0 the free-electron rest mass, being 9.11×10^{-31} kg.

Soref and Bennett simplified these equations by [40] deriving some empirical expressions that are almost universally used in the literature to evaluate the changes caused by injection or depletion of free carriers in silicon at a wavelength of 1300 nm [30]:

$$\Delta\alpha = -[6.0 \times 10^{-18}\Delta N_\mathrm{e} + 4.0 \times 10^{-18}\Delta N_\mathrm{h}], \tag{15}$$

$$\Delta n = -[6.2 \times 10^{-22}\Delta N_\mathrm{e} + 6.0 \times 10^{-18}\Delta N_\mathrm{h}^{0.8}]. \tag{16}$$

Similar expressions have also been derived for 1550 nm [30]:

$$\Delta\alpha = -[8.5 \times 10^{-18}\Delta N_\mathrm{e} + 6 \times 10^{-18}\Delta N_\mathrm{h}], \tag{17}$$

$$\Delta n = -[8.8 \times 10^{-22}\Delta N_\mathrm{e} + 8.5 \times 10^{-18}\Delta N_\mathrm{h}^{0.8}]. \tag{18}$$

The subscripts e and h denote electrons and holes, respectively. Since the number of electrons and holes created by TPA are equal, $N_\mathrm{e}(t, z)$ and $N_\mathrm{h}(t, z)$ can be replaced by $N(t, z)$ (in units of cm^{-3}) in equations (15)–(18).

The empirical relations are in good agreement with the classical Drude–Lorenz model described earlier. However, for the influence of holes on the refractive index Soref *et al* included a $N_\mathrm{h}^{0.8}$ dependence. From equation (17) the FCA cross section σ_FC in cm^2 for silicon at $\lambda = 1.55\,\mu$m can be derived [38]:

$$\sigma_\mathrm{FC} = 1.45 \times 10^{-17}\left(\frac{\lambda}{1.55}\right)^2, \tag{19}$$

where the constant represents the experimentally determined cross section obtained by Soref *et al* The quadratic term is a scaling factor where λ is the wavelength of the incident photon which is expressed in micrometres here. This equation reveals that the apparent cross section of the free-carriers scales with wavelength. The decrease in optical intensity I as a function of propagation distance z as a result of the free-carrier absorption can be written as

$$\frac{\mathrm{d}I}{\mathrm{d}z} = -\sigma_\mathrm{FC} N_\mathrm{FC} I, \tag{20}$$

where N_FC is the free-carrier density. Being induced by a strong pump signal, both the TPA and FCA processes induced by strong pump signals cause absorption of the pump signal itself, and consequently self-limiting of the transmitted optical power. For example, figure 3 shows the output intensity of 200 fs pulses with a centre wavelength of 1700 nm as they pass through a silicon wire waveguide with a cross section of 300 nm × 400 nm. Clearly these absorption processes play a dominant role for input powers >0.5 mW in this particular experiment as one sees a marked decrease in the transmission percentage. Similar data has been presented by Cowan *et al* [41] who used 100 fs laser pulses. The effects of TPA and FCA on pulses with 300 fs, 3.5 ps and 17 ns will be theoretically discussed in section 3.1.1; our results are presented in figure 9.

In the presence of weaker probe pulses, the absorption can be exploited for XAM, an effect which is discussed in section 2.4.1.

The change in refractive index and absorption due to free-carrier injection, either by current injection or by TPA,

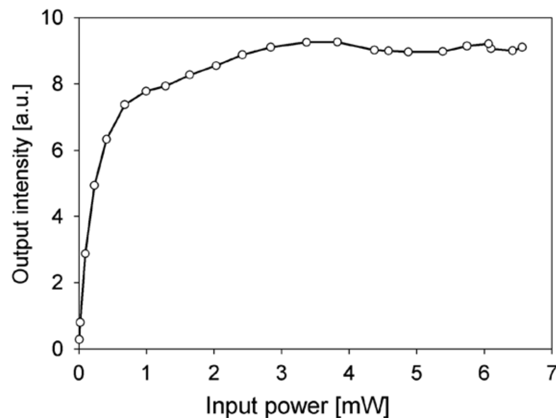

Figure 3. Experimentally observed pump saturation as a function of the average power coupled into a SOI photonic wire.

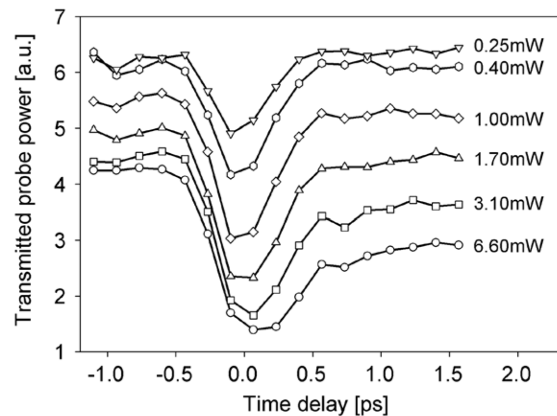

Figure 4. Experimental demonstration of TPA and FCA in a silicon waveguide with a cross section of 300 × 450 nm using 200 fs pulses. The values at the right of the plots indicate the average optical power inside the waveguide.

can effectively be exploited, for example in the fabrication of fast modulators [42, 43] and switches [44]. Free-carrier injection by photo-excitation has also been exploited in silicon microring resonators to demonstrate all-optical switching by detuning the resonance wavelength of the resonator [45–47]. However, the switching speed of such resonators is limited by the quality factor and the free-carrier lifetimes. The latter can be effectively controlled using p-i-n junctions, as demonstrated by Preble *et al* [42]. A drawback of free-carrier induced refractive index changes in resonant structures is that it can cause bistable operation [48], which is not always desirable. Yet, bistable properties can be exploited in applications where pulsating behaviour at the output ports is wanted [49]. Optical pulses of 100 ns with MHz repetition rates have been predicted by Johnson *et al* [50] due to thermo-optic bistability in silicon microdisk resonators at input powers of 60 μW.

In addition to microring resonators other photonic crystal structures have also been used to demonstrate all-optical switching by detuning the optical bandgap through carrier injection [51, 52]. As a consequence of their resonant behaviour, photonic crystals are also prone to bistable operation [53, 54], in a similar way as microring resonators.

All-optical switching in non-resonant structures has been achieved through photo-induced carrier injection in one of the arms of a directional coupler [55] or Mach–Zehnder interferometer [24]. Furthermore, a photonic read-only memory based on the free-carrier effects has recently been proposed by Barrios *et al* [56].

2.3. The optical Kerr effect

The optical Kerr effect is responsible for the intensity dependent refractive index n_2 and is related to the real part of $\chi^{(3)}$ through [57, 58]:

$$n_2 = \frac{3\chi^{(3)}_{\mathrm{Re}}}{4c\varepsilon_0 n_0^2}. \tag{21}$$

The Kerr effect causes the refractive index of a material to be linearly dependent on the optical intensity I, according to

$$n(I) = n_0 + n_2 I, \tag{22}$$

which is similar to the absorption increase described in equation (10).

In many articles the value for n_2 is expressed in electrostatic units (esu). We refer to the definition used by Samoc *et al* [59] and DeSalvo *et al* [60] to convert between esu and SI units:

$$n_2(\mathrm{SI}) = \frac{40\pi}{cn_0} n_2'(\mathrm{esu}). \tag{23}$$

Reported values for n_2 range from 4×10^{-14} to $9 \times 10^{-14}\,\mathrm{cm}^2\,\mathrm{W}^{-1}$ [25, 26] and are frequently determined using the well-known Z-scan technique [26]. Among other applications the Kerr nonlinearity can be exploited for the realization of all-optical phase-shifting devices [61] and nonlinear resonators [39].

2.4. Applications

In the following subsections some applications of the third-order nonlinear effects described above are presented.

2.4.1. Cross-absorption modulation The TPA-induced absorption can be applied to modulate a probe signal through a process called XAM. Consider two input signals, *i.e.* a pump and a probe pulse with different frequencies ω_1 and ω_2, respectively; in this case equation (5) simplifies to

$$P^{(3)}(\omega_2) = \varepsilon_0 \frac{3}{2}\chi^{(3)}(-\omega_2; \omega_1, -\omega_1, \omega_2)|E_{\omega 1}|^2 E_{\omega 2}. \tag{24}$$

This non-degenerate TPA process is two times stronger than the degenerate TPA process described in equation (5). This factor of two also holds for the non-degenerate Kerr effect.

Figure 4 shows results obtained from an XAM experiment where the normalized intensity of a weak probe pulse is plotted as a function of the delay time between a high intensity pump pulse and the signal pulse itself. At negative delay times, when the probe pulse is propagating ahead of the pump pulse, there is no change in transmission. However, at zero delay time, the probe pulse experiences both TPA and FCA and hence the absorption is maximized. At positive delay times the probe

pulse experiences losses due to FCA. The free-carrier lifetime can be obtained by fitting an exponential decay curve through the tail at positive delay times. The time to switch the probe signal 'OFF' is related to the pump pulse envelope, whereas the pump peak intensity determines the 'ON/OFF' ratio. A considerable number of free carriers are generated at high 'ON/OFF' ratios; this can be seen in figure 4. The time needed to switch the probe signal 'ON' again is determined by the free-carrier lifetime. Therefore, for fast all-optical modulation it is desirable to engineer the waveguide such that the free-carrier lifetime is reduced (section 4.2) or to otherwise limit or prevent free-carrier generation (section 3.1). An alternative method is to electrically sweep the generated free carriers out of the waveguide using PN junctions, similar to devices where free carriers are injected on purpose for electrically driven modulation [30, 62]. This method was most notably used to realize the first continuous-wave Raman silicon laser [63].

Ultrafast all-optical switching was demonstrated by modulation of a CW signal through non-degenerate TPA using 3.2 ps pulses by Liang *et al* [32]. A high-speed all-optical NOR gate based on non-degenerate TPA has recently been demonstrated as well [64].

It should be noted that both TPA and FCA will increase the temperature of the silicon; however, modelling has shown that FCA-induced heating dominates the heating due to TPA [50]. Furthermore, the recombination of the free carriers may lead to additional heating [7]. Of course a change in temperature will also induce a change in the refractive index. At 1550 nm the refractive index change associated with Si may be approximated by [65]

$$\frac{\mathrm{d}n}{\mathrm{d}T} = 1.86 \times 10^{-4}/K. \tag{25}$$

A model for the values for $\mathrm{d}n/\mathrm{d}T$ as a function of temperature and wavelength was presented by Ghosha [66]. The positive change in the refractive index is opposite to the refractive index change caused by the free carriers. Although thermal effects in silicon are typically slow compared with electro-optical effects and free-carrier effects, they can be efficiently used to tune the resonance frequency of a microring resonator [67] when ms tuning is acceptable.

2.4.2. Phase modulation The refractive index changes caused by both the optical Kerr effect and free carriers cause a change in the phase of an optical signal. In the next section we discuss two approaches to realize all-optical phase modulation, i.e. phase modulation that is exerted on the signal itself (known as SPM) and phase modulation acting on another signal (known as XPM).

2.4.3. Self-phase modulation As a consequence of the Kerr-nonlinearity and any generated free carriers, the refractive index of a material is dependent on the optical power. When a strong light pulse passes through a medium it will induce a phase shift $\Delta\phi$ due to these nonlinearities. Under CW operation the intensity and phase change can be assumed constant as a function of time. However, when ultrashort pulses are used the intensity rapidly varies in time which results in a rapidly varying phase change. The time derivative of the phase change yields a frequency chirp, $\Delta\omega$ (schematically shown in figure 5), across the pulse, according to:

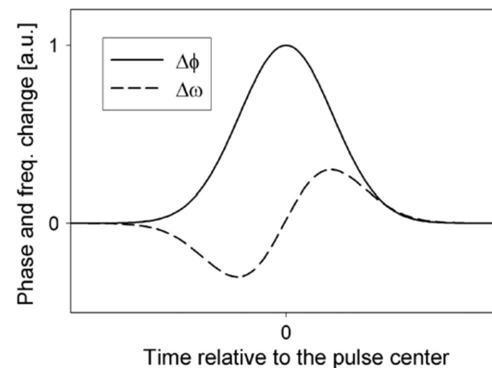

Figure 5. Schematic representation of the normalized induced phase change and frequency shift due to the optical Kerr effect.

$$\Delta\omega = -\frac{\mathrm{d}(\Delta\phi)}{\mathrm{d}t}. \tag{26}$$

A chirped pulse (figure 5) is spectrally broader than an unchirped pulse since its rising edge sees a positive $\mathrm{d}(\Delta\phi)/\mathrm{d}t$ (in the case of a pure Kerr nonlinearity), whereas the trailing edge experiences the opposite phase change, resulting in a red and blueshift, respectively. A rough estimation of the induced phase shift expressed in units of π can be obtained by counting the number of peaks in the output spectrum. Figure 6 shows examples of experimentally observed and simulated SPM broadened spectra (derived by solving the nonlinear Schrödinger equation described later in section 3.2.1) at several points in a waveguide of length L, resulting in an increased phase shift as a function of propagation length.

A careful analysis of the effect of self-phase modulation on 1.8 ps pulses in submicrometre silicon waveguides was recently presented by Dulkeith *et al* [22]. They investigated the spectral broadening of picosecond pulses as a function of power and wavelength during propagation through a Si waveguide. SPM of subpicosecond pulses in silicon wires has been reported by Dekker [21], Hsieh [68] and Boyraz *et al* [20]. The latter reported spectral broadening due to SPM of 4 ps pulses as well.

An all-optical modulator has been demonstrated based on filtering of an SPM broadened spectrum of 100 fs pulses using an integrated Bragg grating [41]. At low powers the pulse is simply reflected by the grating. As the pulse spectrum broadens at increasing powers, however, the new spectral components in the tails of the spectrum overlap with the passband of the grating and are transmitted.

2.4.4. Cross-phase modulation In SPM new frequency components are created within a strong pump pulse, since the pulse temporally overlaps with the refractive index change it has induced upon itself. However, the refractive index change not only affects the pump pulse, but it can also alter a probe pulse, when present, by inducing a phase change in the probe. This non-degenerate process is called cross-phase modulation (XPM) since the phase of the probe pulse is influenced by the pump pulse (strictly speaking the pulses can have any strength).

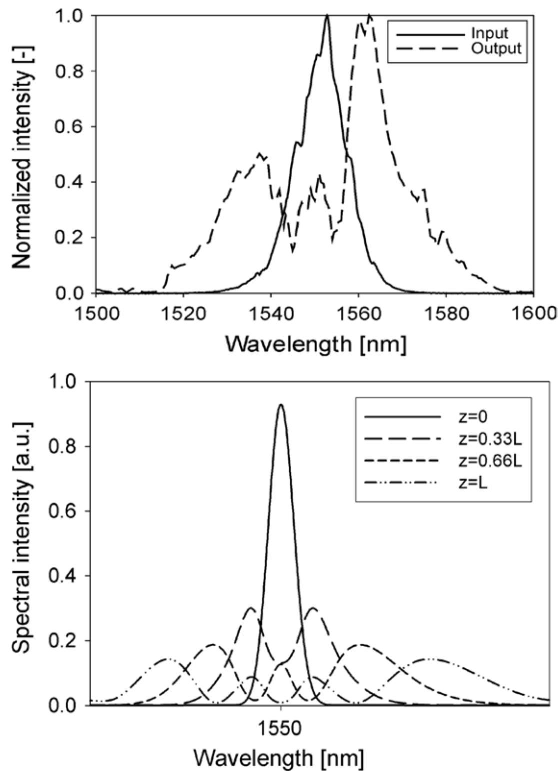

Figure 6. Top: experimentally observed SPM broadened spectrum, taken from [21]. Bottom: simulation results of the resulting wavelength spectrum as a function of propagation length due to the Kerr nonlinearity. The scale along the horizontal axis is intentionally blank. The pulse spectrum typically broadens from 15 nm to 100 nm for 300 fs (FWHM) pulses (with average powers of $\sim$500 μW) propagating through a 1 cm SOI waveguide.

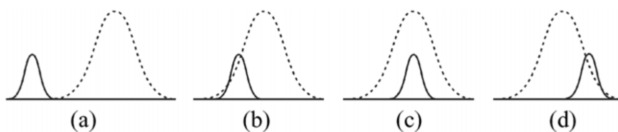

Figure 7. Schematic representation of pump–probe pulses that overlap in time. The dashed curve represents the high intensity pump pulse, whereas the solid line represents the much weaker probe pulse.

XPM can be used for all-optical switching and modulation in different ways. One method is based on a phase change induced in one of the arms of a Mach–Zehnder interferometer. Boyraz *et al* [24] reported all-optical switching based on constructive and destructive interference exploiting cross-phase modulation of a CW signal in a Mach–Zehnder interferometer. Although the optical pump beam produced subpicosecond pulses, the off-switching time in their experiments was limited to $\sim$7 ns, as a result of the free-carrier lifetime.

An alternative way to exploit XPM for all-optical switching is to use the wavelength shift of the probe pulses which is induced by the pump pulses.

Four different configurations are shown in figure 7 in order to illustrate the principle of XPM induced wavelength conversion. It is important to correctly define the time axis when depicting pump–probe experiments and in figure 7 the left sides of the pulses are passing earlier in time than the right side of the pulses. This means that in figure 7(a) the probe pulse is propagating ahead of the pump pulse and does not feel any influence of the pump pulse. Therefore, nothing happens to the spectral distribution of the probe spectrum. However, in (b), when the probe is overlapping with the leading edge of the pump pulse, it is influenced by the positive change in the refractive index as a function of time $\mathrm{d}(\Delta n)/\mathrm{d}t$, which in turn generates a positive phase change $\mathrm{d}(\Delta\phi)/\mathrm{d}t$. This positive change of the phase induces a decreased carrier frequency, which results in an increase of the centre wavelength of the probe. In other words, the probe spectrum red shifts. In configuration (c) the probe pulse is exactly centred within the pump pulse and therefore it overlaps with both the leading and trailing edge of the pump pulse. In this case the induced phase changes will more or less compensate each other (depending on the dispersion properties of the waveguide) and the shift of the wavelength will be zero. Finally, in figure 7(d) the probe overlaps with the trailing edge of the pump and consequently experiences a negative refractive index change, resulting in a blue shift of the probe carrier wavelength.

Xu *et al* [18] reported a 1.6 nm blue shift of a CW probe signal due to the XPM induced by using 3.5 ps pump pulses. They exploited the wavelength shift to demonstrate all-optical switching by using a tunable grating filter at the output of the waveguide. Since the wavelength conversion scales with the slope of the pulse envelope, larger wavelength shifts can be obtained by increasing the peak pulse intensity and by decreasing the pulse duration. Dekker *et al* [23] reported sub-picosecond all-optical wavelength conversion through XPM using 300 fs pulses, resulting in wavelength shifts ranging from -15 to 9 nm with 7.5 pJ pulse energies. They proposed an all-optical switching and modulation scheme using XPM induced wavelength conversion in a straight silicon port waveguide and subsequent filtering of the wavelength converted signal by an integrated low-Q passive silicon microring resonator. An experimental demonstration of this device has recently been presented by Dekker *et al* [69].

The wavelength shift of the probe in pump–probe experiments depends not only on the pump intensity but also on the length over which the pump and probe pulses overlap, i.e. the interaction length. Since submicrometre silicon waveguides are strongly dispersive, the probe pulse, in general, travels at a different speed in comparison with the pump pulse. The propagation length over which the pump and probe pulses overlap is termed the walk-off length L_w. This walk-off length is a linear scaling factor for the magnitude of the XPM induced probe wavelength shift. Its relation to the dispersion of the waveguide is presented in section 4.4.

2.4.5. Four-wave mixing Four-wave mixing is a nonlinear effect that also arises from the third-order optical nonlinearity. It can occur if at least two different frequency components, ω_1 and ω_2, propagate in a nonlinear medium. A refractive index modulation at the difference frequency is obtained, which creates sidebands for each of the input waves. As a result, two new frequency components are generated (figure 8), namely, $\omega_3 = \omega_1 - (\omega_2 - \omega_1) = 2\omega_1 - \omega_2$ and $\omega_4 = \omega_2 + (\omega_2 - \omega_1) = 2\omega_2 - \omega_1$.

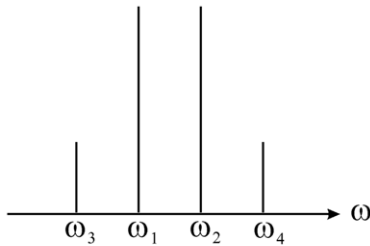

Figure 8. Generation of new frequency components via four-wave mixing.

To describe the generation of ω_3, equation (5) can be rewritten as

$$P^{(3)}(2\omega_1 - \omega_2) = \varepsilon_0 \frac{3}{4} \chi^{(3)}(-2\omega_1 + \omega_2; \omega_1, \omega_1, -\omega_2) E_{\omega 1} 2 E^*_{\omega 2}. \quad (27)$$

FWM is a phase-sensitive process in which the interaction depends on the relative phases of all the involved beams; it can only accumulate over a non-negligible distance when a phase-matching condition ($k_{2\omega_1-\omega_2} = 2k_{\omega_1} - k_{\omega_2}$) is satisfied. This occurs when the involved frequencies are close to each other, or when the dispersion profile has an appropriately engineered shape (see section 4.4). In other cases, where there is a strong phase mismatch, FWM is effectively suppressed. The phase-matching requirement for FWM may be contrasted with TPA and the Kerr effect, which are automatically phase-matched [7] and Raman scattering which does not require phase matching. Despite the added complexity imposed by phase matching, FWM can be exploited for broadband signal amplification and frequency conversion [25,70–73]. Foster *et al* [74] demonstrated net gain over a wavelength range of 28 nm and frequency conversion through FWM with peak conversion efficiencies of +5.2 dB using phase-matched SOI nanowires. Furthermore, Lin and Agrawal proposed to use FWM for the generation of quantum correlated photon pairs [75].

2.5. Stimulated raman scattering

The nonlinear response of a transparent optical medium to the intensity of the light propagating through the medium is very fast, but not instantaneous. In particular, a non-instantaneous response is caused by vibrations of the crystal (or glass) lattice. When these vibrations are associated with optical phonons, the effect is called Raman scattering, while acoustical phonons are associated with Brillouin scattering. When, for example, two laser beams with a frequency difference matching a Raman transition propagate together through a Raman-active medium, the longer-wavelength beam can experience optical gain at the expense of the shorter-wavelength beam. In addition, lattice vibrations are excited which leads to a temperature increase. The gain for the longer-wavelength beam is commonly used in Raman amplifiers and Raman lasers. Apart from the mentioned stimulated Raman scattering effect, there is also a spontaneous Raman scattering effect caused by quantum noise. One may interpret this as Raman amplification of vacuum noise. In solid state media, like silicon, the Raman effect occurs together with the Kerr effect, which results from the (nearly) instantaneous response of the electrons.

In SOI waveguides, which are based on single crystalline silicon, the Raman transition is dominated by a single peak at ∼520 cm^{-1} [76] having a spectral width of ∼0.9 nm [77]. This narrow gain spectrum is beneficial for laser operation, but results in a significant drawback for broadband amplification of optical signals on a silicon chip. The width of the Raman peak broadens and shifts to lower values in very thin silicon nanowires with diameters below 20 nm [78]. Furthermore, the width and position of the Raman peak tends to broaden [79] and shift to slightly lower values compared with single crystalline silicon in the case of polycrystalline and amorphous material structures [80–82].

The generation of free carriers strongly hinders gain performance [16,36–38,83] and should be avoided or limited when designing amplifiers, similar to the case of ultrafast all-optical modulation using TPA, as discussed in section 2.2. Reducing the free-carrier lifetime is one technique that can be used to decrease the free-carrier concentration. Jalali *et al* showed the impact of the free-carrier lifetime on the achievable CW Raman gain as a function of pump intensity [35]. The monolithic integration of p-i-n diode structures has also been successfully applied to sweep out the generated free carriers in order to reduce the free-carrier concentrations [34, 63, 84].

For more information on the physics of Raman effects and Raman amplification in silicon we refer the interested reader to the works of Xu *et al* [18, 77], Espinola *et al* [85], Dadap *et al* [86] and Claps *et al* [87]

3. Modelling methods

In this section we discuss two approaches commonly used to model the propagation of short optical pulses in silicon waveguides. The first method, described in section 3.1, describes the propagation of an intensity profile in the time domain. Since this approach propagates an intensity profile, it is not able to include dispersion. Therefore, this model is only suitable for propagation of pulses through short waveguides that show little dispersion. Nevertheless, it gives good insight into the temporal distortion of the pulse under the influence of both TPA and FCA. Based on this simple model, numerical results of femtosecond, picosecond and nanosecond pulse propagation in SOI waveguides are presented and compared with recent experimental data from the literature. For instance, an indication of the XPM induced wavelength shift can be derived based on the temporal shape of the pump pulse.

The second method, which is more extensive and described in section 3.2, is based on the nonlinear Schrödinger equation (NLSE). The NLSE is solved using the split-step Fourier method. This method includes the dispersive effects of the waveguide, provides a means by which to study the effects of phase matching and may also be extended to incorporate Raman effects.

For both methods it is important to know the initial shape of the pulse in the time domain; typically a Gaussian or hyperbolic-secant shaped pulse is assumed. The spectral distribution of the pulse is then obtained by Fourier transforming the optical field during the pulse's evolution in the time domain. In this paper we assume the pulse shapes are Gaussian for simplicity.

Table 1. Parameters used in the simulations of section 3 for pulse propagation in different SOI waveguides and pulse durations.

Par	300 fs	3.5 ps	17 ns
Ref	[23]	[18]	[17]
$w \times h$	450 nm × 300 nm	450 nm × 250 nm	1520 nm × 1450 nm
A_{eff}	$\sim 0.15\ \mu\mathrm{m}^2$	$\sim 0.14\ \mu\mathrm{m}^2$	$\sim 1.5\ \mu\mathrm{m}^2$
L	7 mm	7 mm	48 mm
τ	5 ns	5 ns	25 ns
I_{max}	$\sim$15 GW cm^{-2}	$\sim$15 GW cm^{-2}	$\sim$50 MW cm^{-2}
F_{rep}	80 MHz	76.8 MHz	10 KHz
λ_{p}	1554 nm	1589.5 nm	1545 nm
λ_{s}	1683 nm	1731.5 nm	1680 nm

Furthermore, it should be noted that both methods assume that individual pulses are separated in time and are not influenced by the presence of a free-carrier background; the number of free carriers generated by a previous pulse are assumed to have diminished to a negligible level when the next pulse passes through the device. For a repetition rate of 80 MHz this would require the free-carrier lifetime to be less than 12.5 ns, which is often the case for submicrometre shaped silicon wire waveguides.

3.1. Dispersion free propagation

3.1.1. Single wavelength experiments — pump pulses We begin by assuming a Gaussian intensity profile

$$I(t) = I_{\mathrm{max}} \exp\left(-0.5.\left(\frac{|t-t_0|}{\delta}\right)^2\right) \tag{28}$$

is incident on the input facet of a SOI waveguide where I_{max} is the peak power of the pulse (in W m^{-2}), t represents time and t_0 is the centre location of the pulse (in seconds) and δ characterizes the pulse width.

During propagation through the waveguide, where the propagation direction is coincident with the z-axis, the intensity of the pulse $I(t, z)$ decreases due to several loss mechanisms. These loss mechanisms include linear absorption including scattering, TPA and FCA. Therefore, the change in pump intensity along the waveguide may be described by [17]

$$\frac{\mathrm{d}I(t,z)}{\mathrm{d}z} = -\alpha I(t,z) - \beta I^2(t,z) - \sigma N(t,z)I(t,z), \tag{29}$$

where α is the linear absorption, $N(t, z)$ is the free-carrier density and σ is the free-carrier absorption cross section described in equation (19). Because the losses are a function of time, via the free-carrier density $N(t, z)$ and the pulses intensity profile $I(t, z)$, the original pulse shape is not conserved during propagation through the waveguide. The time dependence of the free-carrier density in a silicon waveguide can be written in terms of electron–hole pair generation and recombination rates [17] (see equation (7)), however, it now also depends on the propagation distance z and can be generalized to

$$\frac{\mathrm{d}N(t,z)}{\mathrm{d}t} = \frac{\beta}{2h\nu}I^2(t,z) - \frac{N(t,z)}{\tau}. \tag{30}$$

The set of coupled differential equations, equations (29) and (30), can be solved numerically by dividing the waveguide into discrete propagation steps dz. The results of a discretization of the pulse shape $I(t, z)$ into finite time steps dt can be stored in a two-dimensional array that holds the pulse shape as a function of propagation distance z. The carrier density $N(t, z)$ can be stored in a similar fashion as $I(t, z)$. As a starting condition the original pulse is used to fill array $I(t, 0)$ and $N(t, 0)$ is determined by using $I(t, 0)$ in equation (30). This is valid when dz is chosen small enough that errors are minimized, a condition that can be verified by reducing dz until the solution no longer depends on dz. Using this approach, equations (29) and (30) can be solved alternatively within a single step of size dz. This straightforward method generates two data arrays that hold the predicted pulse intensity and carrier-density as a function of time and position within the waveguide. Some examples of the results obtained by using this method are presented in figures 9–11 for pulse durations of 300 fs, 3.5 ps and 17 ns, respectively. The input parameters for these simulations are listed in table 1.

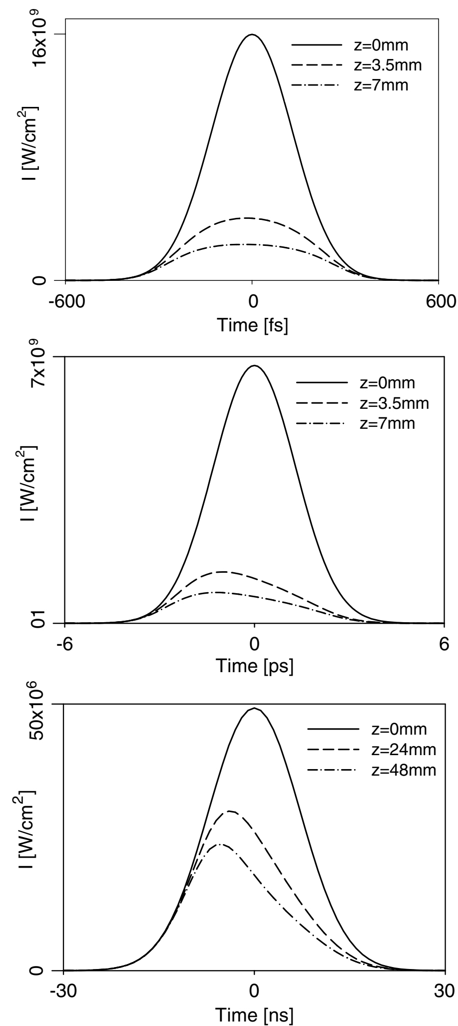

Figure 9. Pulse envelopes as a function of propagation distance. Top: 300 fs pulses. Middle: 3.5 ps pulses. Bottom: 17 ns pulses.

In figure 9 we are able to conclude that the nonlinear losses for the 300 fs pulses are dominated by TPA, since the losses are almost symmetric around the pulse centre. However, as the pulse length is increased to 3.5 ps the additional losses

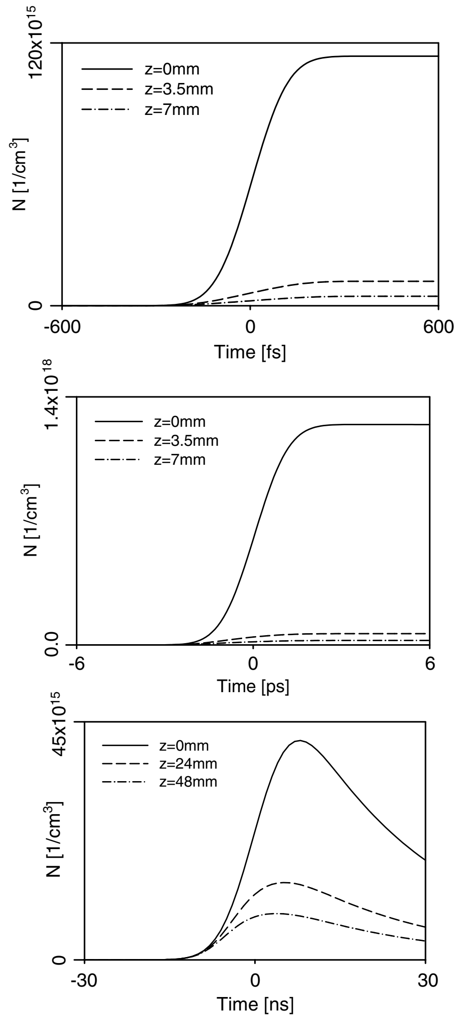

Figure 10. Free carrier densities as a function of propagation distance. Top: 300 fs pulses. Middle: 3.5 ps pulses. Bottom: 17 ns pulses.

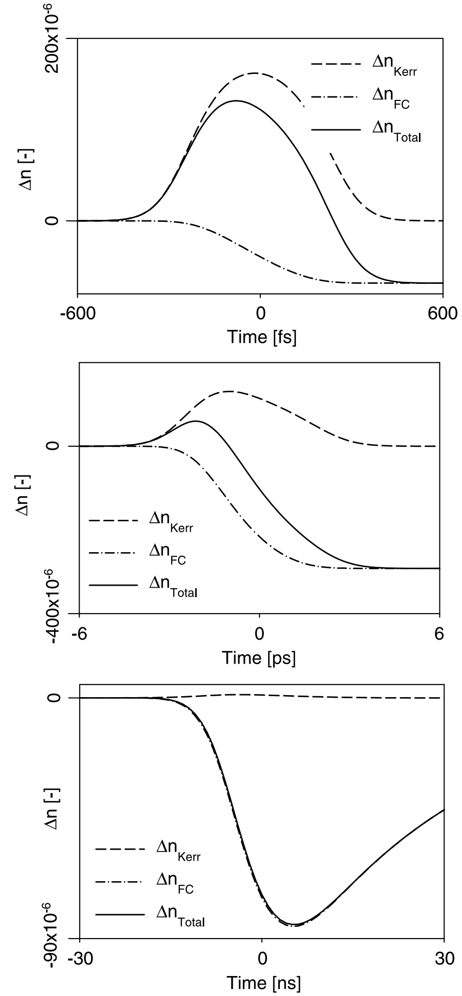

Figure 11. Kerr- and free-carrier-induced refractive index changes as a function of propagation distance. Top: 300 fs pulses. Middle: 3.5 ps pulses. Bottom: 17 ns pulses.

due to FCA become more prominent. This causes a stronger absorption for the trailing pulse edge due to the free-carrier buildup experienced during the pulse's leading edge and centre. When an even longer pulse duration of 17 ns is used, the losses are dominated by FCA, which can be concluded from the fact that the leading edge is not strongly attenuated and the peak intensity is only weakly influenced by the propagation length.

The time-dependent free-carrier densities generated by the three different pulses of figure 9 are shown in figure 10.

From figure 10 it can be seen that the free-carrier accumulation for a 300 fs pulse is an order of magnitude lower than it is for a 3.5 ps pulse. Therefore, the Kerr nonlinearity dominates over the free-carrier nonlinearities for subpicosecond pulses. This conclusion has also been experimentally confirmed by Hsieh *et al* [68] who studied SPM and dispersion effects in SOI wire waveguides using 200 fs pulses and by Boyraz *et al* [20] who used <1 ps pulses. Through these simple simulations we also find that although the carrier densities for the 17 ns pulses are the lowest (one order of magnitude lower than those experienced by the 300-fs pulses), they cause considerable loss since the pulse duration is four orders of magnitude longer. This causes a stronger overlap between the pulse and the carriers it has generated.

3.1.2. Pump–probe experiments Short pulses propagating through a silicon waveguide experience not only loss but also refractive index changes caused by the Kerr effect and the generated free carriers. The Kerr-induced refractive index change as a function of time and propagation distance is described by

$$\Delta n_{\mathrm{Kerr}}(t,z) = n_2 I(t,z), \tag{31}$$

where a value of $n_2 = 4 \times 10^{-14}\,\mathrm{cm^2\,W^{-1}}$ has been used in the simulations shown in figure 11. The free-carrier induced refractive index change carries a negative sign and can be described by the empirical relation presented by Soref *et al* [40]:

$$\Delta n_{\mathrm{FC}}(t,z) = -(8.8 \times 10^{-22} N_{\mathrm{e}}(t,z) + 8.5 \times 10^{-18} N_{\mathrm{h}}(t,z)^{0.8}). \tag{32}$$

The Kerr- and free-carrier-induced refractive index changes of the 300 fs, 3.5 ps and 17 ns pulses presented in section 3.1.1. are shown in figure 11 according to equations (31) and (32).

From figure 11 it can be concluded that the Kerr nonlinearity dominates over the free-carrier-induced refractive index for subpicosecond pulses. We also find that the effects are balanced for the 3.5 ps pulse, while for the 17 ns pulse the Kerr effect is negligible.

Next, we consider a pump–probe experiment where the delay time between the pulses is such that the probe signal has a temporal overlap with the pump signal on either the rising or trailing edge, as shown by the cartoon in figure 7(*b*) or in figure 7(*d*). In this case, the probe signal will experience a time-dependent phase shift $\Delta\phi(t,z)$ caused by the temporal change in the pump–pulse induced index changes [18] via

$$\Delta\phi(t,z) = \frac{2\pi L_{\mathrm{int}}}{\lambda}[\Delta n_{\mathrm{Kerr}}(t,z) + \Delta n_{\mathrm{FC}}(t,z)], \qquad (33)$$

where L_{int} is the interaction length. This temporal variation in phase will result in a frequency shift of the probe pulses according to

$$\Delta\omega(t,z) = -\frac{\mathrm{d}}{\mathrm{d}t}\Delta\phi(t,z). \qquad (34)$$

This frequency shift changes the centre wavelength of the probe pulses and can be described by [23]

$$\lambda_{\mathrm{s}} = \frac{\lambda_0}{1-(L_{\mathrm{int}}/c)\cdot(\mathrm{d}\Delta n(t,z)/\mathrm{d}t)}, \qquad (35)$$

where λ_{s} is the centre wavelength of the frequency converted probe pulse and λ_0 represents the centre wavelength of the original probe spectrum.

Although not exact, a good indication of the wavelength shift can be derived from the slope of the refractive index profiles shown in figure 11. The wavelength shifts for the three different pulse lengths previously examined have been derived using equation (35) at the middle of the waveguide and are shown in figure 12. A comparison with experimental data is presented in figure 13.

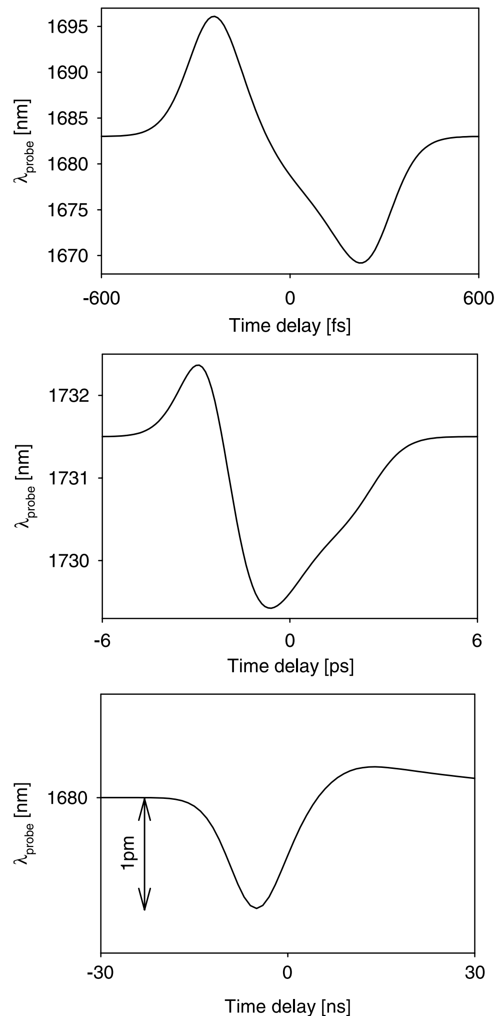

Figure 12. Predicted wavelength shifts as a function of delay time between pump and probe pulses. Top: 300 fs pulses. Middle: 3.5 ps pulses. Bottom: 17 ns pulses.

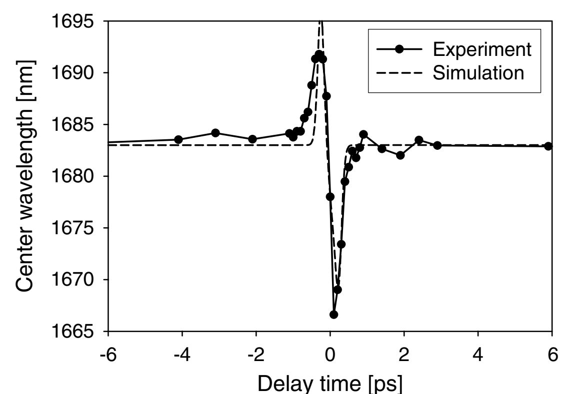

Figure 13. Experimental and simulated wavelength shift for 300 fs pulses through SOI wire waveguides with a cross section of 300 nm × 450 nm and a length of 7 mm. Pulse energy was 7.5 pJ. Taken from [23].

3.2. Modeling including dispersion — NLSE

The modelling approach described in section 3.1 gives good insight into the dynamics of the pulse intensity. However, as pulse durations and waveguide dimensions decrease, dispersive effects become increasingly important and must be taken into account. A convenient model that describes nonlinear pulse propagation in a waveguide is the Nonlinear Schrödinger Equation. In the next two subsections this equation will be applied to model both single-pulse propagation experiments and pump–probe experiments.

3.2.1. Single wavelength experiments — pump pulses The propagation of short electromagnetic pulses inside a channel waveguide with Kerr nonlinearities, TPA and dispersion can be described by a modified nonlinear Schrödinger equation [88–90]:

$$\begin{aligned}\frac{\mathrm{d}\psi}{\mathrm{d}z} = &-\frac{\mathrm{i}}{2}\cdot\beta_2\cdot\frac{\mathrm{d}^2\psi}{\mathrm{d}\tau^2}+\frac{\mathrm{i}}{6}\cdot\beta_3\cdot\frac{\mathrm{d}^3\psi}{\mathrm{d}\tau^3}+\frac{\mathrm{i}}{24}\cdot\beta_4\cdot\frac{\mathrm{d}^4\psi}{\mathrm{d}\tau^4}\\ &-\frac{1}{2}\cdot\alpha_0\cdot\psi-\frac{\alpha_{\mathrm{TPA}}}{A_{\mathrm{eff}}}|\psi|^2\psi+\mathrm{i}\cdot\gamma|\psi|^2\psi\\ &-\frac{\gamma}{\omega_0}\cdot\frac{\mathrm{d}}{\mathrm{d}\tau}(|\psi|^2\psi)-\mathrm{i}\cdot\gamma\cdot T_{\mathrm{R}}\cdot\psi\cdot\frac{\mathrm{d}}{\mathrm{d}\tau}(|\psi|^2), \qquad (36)\end{aligned}$$

where $\psi(z,\tau)$ represents the slowly varying complex envelope of the optical field. The shape of the electric-field envelope as a function of propagation distance $\psi(z,\tau)$ can be found by solving equation (36). A convenient way to solve this

Table 2. List of terms in the nonlinear Schrödinger equation.

Term	Description
$\frac{d\psi}{dz}$	Change of the slowly varying complex pulse envelope with propagation z
$-\frac{i}{2}\cdot\beta_2\cdot\frac{d^2\psi}{d\tau^2}$	Group velocity dispersion
$\frac{i}{6}\cdot\beta_3\cdot\frac{d^3\psi}{d\tau^3}$	Third-order group velocity dispersion (becomes important for pulses with large bandwidths)
$\frac{i}{24}\cdot\beta_4\cdot\frac{d^4\psi}{d\tau^4}$	Fourth order group velocity dispersion (becomes important for pulses with large bandwidths)
$-\frac{1}{2}\cdot\alpha_0\cdot\psi$	Linear propagation losses
$-\frac{\alpha_{TPA}}{A_{eff}}\lvert\psi\rvert^2\psi$	Two photon absorption (TPA)
$i\cdot\gamma\lvert\psi\rvert^2\psi$	Self phase modulation (SPM)
$-\frac{\gamma}{\omega_0}\cdot\frac{d}{d\tau}(\lvert\psi\rvert^2\psi)$	Self-steepening and shock formation
$-i\cdot\gamma\cdot T_R\cdot\psi\cdot\frac{d}{d\tau}(\lvert\psi\rvert^2)$	Intrapulse Raman scattering

equation is to make use of the well-known split-step Fourier method (SSFM), which is explained later in this section. In equation (36) γ is the nonlinear parameter, which can be expressed as

$$\gamma = \frac{2\pi}{\lambda}\times\frac{n_2}{A_{eff}} = \frac{\omega_0}{c}\times\frac{n_2}{A_{eff}} = k_0\times\frac{n_2}{A_{eff}}, \qquad (37)$$

where k_0 represents the wave vector. Furthermore, in the modified NLSE, α_0 accounts for propagation losses, α_{TPA} incorporates two-photon absorption and the β_j's represent the higher-order dispersion terms. In this section we introduce α_{TPA} as the TPA coefficient (instead of β) to avoid confusion with the dispersion coefficients β_j. Two other interesting nonlinear terms related to n_2 are γ/ω_0 and $\gamma\cdot T_R$. These terms include the effects of self-steepening or shock formation and an approximate treatment of intrapulse Raman scattering. All the individual terms are summarized in table 2 for convenience.

In order to determine which of the terms listed in table 2 are important for a specific experiment, it is useful to define some characteristic length scales. These lengths, together with their calculated values for the SOI waveguides, described in this section are presented in equations (38)–(45):

$$L_{NL} = \frac{1}{\gamma P_0} = \frac{\lambda A_{eff}}{2\pi n_2 P_0}, \qquad (38)$$

$$L_{D2} = \frac{T_0^2}{\beta_2}, \qquad (39)$$

$$L_{D3} = \frac{T_0^3}{\beta_3}, \qquad (40)$$

$$L_{D4} = \frac{T_0^4}{\beta_4}, \qquad (41)$$

$$L_a = \frac{1}{a_0}, \qquad (42)$$

$$L_W = \frac{T_0}{\lvert d\rvert} = \frac{T_0}{\lvert\beta_{1p}-\beta_{1s}\rvert}, \qquad (43)$$

$$L_S = \omega_0 T_0 L_{NL}, \qquad (44)$$

$$L_{IRS} = \frac{T_0}{T_R}L_{NL}, \qquad (45)$$

where L_{NL} is the nonlinear length, L_{D2}, L_{D3} and L_{D4} are the second-, third- and fourth-order dispersion lengths, L_a is the absorption length, L_w the walk-off length, L_s the shock length and L_{IRS} represents the Raman length. By comparing these length scales to each other or the actual device length L, one can obtain a rough estimate of which terms need to be taken into account in order to construct an accurate model. Intrapulse Raman scattering (IRS) is, in principle, not present in SOI waveguides, because the narrow Raman spectrum is separated from the pulse spectrum by ≈520 cm^{-1}. This means that for a wavelength of 1550 nm, the Raman spectrum is located around 1685 nm. For Gaussian shaped pulses it can be shown that

$$\lambda_{FWHM} = \Delta\lambda = \lambda_0^2\cdot\frac{TBP_{Gaussian}\cdot n}{t_{FWHM}\cdot c}, \qquad (46)$$

where $TBP_{Gaussian}$ is the time-bandwidth product of a transform-limited Gaussian pulse, c is the speed of light in vacuum, λ_0 represents the centre or carrier wavelength and t_{FWHM} is the temporal full-width at half-maximum (FWHM) of the pulse. It should be pointed out that equation (46) is an approximation which is only valid when the spectral width is small compared with the centre wavelength, i.e. $\lambda_{min}\lambda_{max}\approx\lambda_0^2$. Since the time and spectral domains may be related using a Fourier transform, the spectral width of the pulse is inversely proportional to the temporal pulse width. This has the practical consequence that when extremely short pulses are used, the Raman phonons excited by the shorter wavelengths that are present in the broad pulse spectrum might interact with the longer wavelengths within the pulse. However, we point out that this is generally only important when, for example, a transform- limited pulse has a width below 30 fs.

In most cases, modified NLSE's cannot be solved analytically. Therefore, numerical methods are needed when nonlinear effects are present. Several approaches can be used such as the finite-difference time-domain (FDTD) method, the inverse scattering method, various perturbation techniques, Runge–Kutta schemes, or the split-step fourier method (SSFM). In general, the latter approach is the most efficient because of its inherent stability and reasonable calculation speeds, and as a consequence we will discuss its application in more detail. To use the SSFM, an appropriate temporal discretization is needed; this leads to a system of ordinary differential equations [90] with both higher-order linear terms and nonlinear terms:

$$\frac{\partial\tilde{A}}{\partial z} = \tilde{L}\tilde{A} + \tilde{N}(\tilde{A}). \qquad (47)$$

The split step method is based on splitting the equation into a linear part:

$$\frac{\partial\tilde{A}}{\partial z} = \tilde{L}\tilde{A} \qquad (48)$$

and a nonlinear part:

$$\frac{\partial\tilde{A}}{\partial z} = \tilde{N}(\tilde{A}), \qquad (49)$$

and solving these equations alternatively. A drawback to this approach is that it makes the assumption that the dispersive and nonlinear effects act independently, however, by choosing a

sufficiently small step size any deleterious consequences can be averted. The numerical approach followed is sketched out here for an asymmetric split step; this is the the simplest split-step scheme, however it is only accurate to first order. To propagate a field A a distance L, under the influence of equation (48), we first determine our spatial resolution by splitting $z = 0 \ldots L$ into n steps of size $h = L/n = 0$. Then equation (49) is solved from 0 to h using the initial condition $A(t, 0)$ the result we obtain is subsequently substituted into equation (48) as the initial condition. In this manor the solution over a short propagation interval for the simple asymmetric split step is approximated by

$$A(z + h, t) = \exp(h\tilde{L}) \exp(h\tilde{N})A(z, t). \qquad (50)$$

The symmetric split step, which is a better choice than the one outlined above since it is globally accurate to second order with only minimal overhead, is used in practice. Although other variations of the split step exist (see, for example, [91]), their discussion is beyond the scope of this paper and ultimately ones accuracy is dictated by the step sizes chosen.

3.2.2. Pump–probe experiments In this section a system of coupled generalized nonlinear Schrödinger equations is presented, which includes the effect of the Raman gain spectrum. Phase-matching terms have been ignored under the assumption that this condition is not satisfied. In these equations we have assumed that the pump and probe pulses may be defined as separate fields, an assumption which requires that the pulses do not spectrally overlap. The equations, which can be solved numerically using a more complicated implementation of the SSFM that includes convolution, follow directly from the work of Headley and Agrawal [92] and Lin *et al* [73]. Similar expressions can also be found in the work of Chen *et al* [93]:

$$\begin{aligned}\frac{d\psi_p}{dz} &= i\sum_{n=1}^{\infty} \frac{i^n\beta_{n_p}}{n!}\frac{d^n}{dt^n}\psi_p - \frac{1}{2}[\alpha_p + \alpha_{FC_p}]\psi_p \\ &+ i\xi_e\left[\gamma + i\frac{1}{2}\beta_{TPA}\right][|\psi_p|^2 + 2|\psi_s|^2]\psi_p \\ &+ i\xi_R\gamma\psi_p\int_{-\infty}^{\infty} g_R(t')[|\psi_p(z, t - t')|^2 + |\psi_s(z, t - t')|^2]\,dt' \\ &+ i\xi_R\gamma\psi_p\int_{-\infty}^{\infty} g_R(t')\psi_p(z, t - t')\psi_s^*(z, t - t')e^{i\Omega_{sp}t'}dt',\end{aligned} \qquad (51)$$

$$\begin{aligned}\frac{d\psi_s}{dz} &= i\sum_{n=1}^{\infty} \frac{i^n\beta_{n_s}}{n!}\frac{d^n}{dt^n}\psi_s - \frac{1}{2}\left[\alpha_s + \alpha_{FC_s}\right]\psi_s \\ &+ i\xi_e[\gamma + i\frac{1}{2}\beta_{TPA}][|\psi_s|^2 + 2|\psi_p|^2]\psi_s \\ &+ i\xi_R\gamma\psi_s\int_{-\infty}^{\infty} g_R(t')[|\psi_p(z, t - t')|^2 + |\psi_s(z, t - t')|^2]\,dt' \\ &+ i\xi_R\gamma\psi_s\int_{-\infty}^{\infty} g_R(t')\psi_s(z, t - t')\psi_p^*(z, t - t')e^{-i\Omega_{sp}t'}\,dt'.\end{aligned} \qquad (52)$$

The terms inside the sum on the right-hand side of equations (51) and (52) take into account the dispersive effects to all orders, with $\beta_{nj} = \beta_n(\lambda_j)$, where $n = 1, 2, 3, \ldots, N$ and $j = p, s$, represents the pump and signal, respectively. Losses are accounted for in the third term; static losses are represented by α_j and the free-carrier absorption by α_{FC_j}. The free-carrier losses are determined by solving

$$\alpha_{FC_j} = 1.45 \times 10^{-17}\left(\frac{\lambda_j}{\lambda_{ref}}\right)^2 N(t, z). \qquad (53)$$

where λ_{ref} is the reference wavelength of 1550 nm and λ_j is the carrier wavelength of the pump and probe fields. For the calculation of the free-carrier concentration $N(t, z)$ we can define the electron-hole pair generation and recombination in a fashion similar to that used in equation (7); however it is now written in terms of the optical field:

$$\frac{dN(t, z)}{dt} = \frac{\xi_e\beta_{TPA}}{2\hbar\omega}\left|\psi_p(t, z)\right|^4 - \frac{N(t, z)}{\tau_{FC}}. \qquad (54)$$

The fourth term in equations (51) and (52) is responsible for the degenerate processes TPA and SPM as well as the non-degenerate processes XAM and XPM. The factor of two for the squared field of the co-propagating signal follows directly from the polarization presented in equation (24), which is twice as strong as the polarization for the degenerate process described by equation (5). The fifth term takes the intrapulse Raman scattering (IRS) and intrapulse cross Raman scattering (XRS) into account. Finally, the sixth and final term is responsible for Raman amplification. In the final two terms $g_R(t)$ is an impulse response function which incorporates the effects of the Raman process in silicon. Although $g_R(t)$ is a material dependent function it may be approximated by a Lorentzian shape in the frequency domain and reasonable agreement may be obtained by using the well-known approximation [91]

$$g_R(t) = \frac{\tau_1^2 + \tau_2^2}{\tau_1\tau_2^2}\exp\left(-\frac{t}{\tau_2}\right)\sin\left(\frac{t}{\tau_1}\right)h(t), \qquad (55)$$

where τ_1^{-1} is the phonon frequency, τ_2^{-1} is related to the bandwidth of the Raman spectrum and $h(t)$ is the heavy-side step function which ensures causality. For silicon these values are $\tau_1 = 10.2$ fs and $\tau_2 = 3.4$ ps. Since it is more convenient to solve this part of the generalized NLSE in the frequency domain, it is useful to express the terms in the frequency domain:

$$g_R(\Omega) = \frac{g_R\Gamma_R\Omega_R}{\Omega_R^2 - \Omega^2 - 2i\Gamma_R\Omega}, \qquad (56)$$

where $g_R = 2 \times 10^{-10}$ m W^{-1} is the Raman gain coefficient at 1550 nm, $\Omega_R/2\pi = 15.6$ THz is the Raman shift (520 cm^{-1}) and the FWHM of the Raman spectrum is given by $\Gamma_R/2\pi = 52.5$ GHz ($\sim$0.9 nm).

The nonlinear refractive index is accounted for through $\gamma = n_2\omega_j/cA_{eff}$ and β_{TPA} is the two-photon absorption coefficient. The coefficients ξ_e and ξ_R describe the electronic and Raman contributions related to the crystal symmetry of the silicon lattice, its orientation with respect to the waveguide and the excited mode [73]. For excitation of a TE mode in a [1 1 0] × [0 0 1] faceted waveguide $\xi_e = 5/4$ and $\xi_R = 1$. However, for excitation of the TM mode $\xi_e = 1$ and $\xi_R = 0$, indicating that Raman effects are not present when the TM

mode is excited. Finally, τ_{FC} is the free-carrier lifetime and $\Omega_{sp} = \omega_s - \omega_p$.

The presence of free carriers changes the refractive index, which could change the relative velocities of the pump and signal in the SOI waveguide causing them to walk off from one another at a different rate than that predicted by the two first-order dispersion terms. This effect will change the pump–probe interaction length in general; however, such changes are likely to be small, since SOI waveguides lengths are typically short (<5 cm). As a consequence, these effects have been ignored in this model. Nevertheless, we point out that such effects can be incorporated in a straightforward manner by using the Drude model, equation (14), or the empirical model from Soref, equations (16) and (18) augmenting the first-order dispersion terms in the above equations.

Equations (51) and (52) can be simplified when it is assumed that the intensity of the pump pulses is much greater than that of the probe pulses, $|\psi_p|^2 \gg |\psi_s|^2$. Furthermore, when modelling pump–probe experiments, probe-induced SPM and probe-induced XPM are negligible and can be ignored. The same holds for the contribution probe pulses have on stimulated Raman scattering. However, the Raman amplification term in the probe equation is important, since we assume that a weak probe can be amplified by stimulated Raman scattering induced by the pump. Under these assumptions the coupled set of NLSEs can be reduced somewhat to

$$\begin{aligned}\frac{d\psi_p}{dz} &= \Delta\frac{d\psi_p}{dt} - i\frac{\beta_{2_p}}{2}\frac{d^2\psi_p}{dt^2} + i\frac{\beta_{3_p}}{6}\frac{d^3\psi_p}{dt^3} - \frac{1}{2}[\alpha_p + \alpha_{FC_p}]\psi_p \\ &+ i\xi_e\left[\gamma + i\tfrac{1}{2}\beta_{TPA}\right]|\psi_p|^2\psi_p \\ &+ i\xi_R\gamma\psi_p\int_{-\infty}^{\infty} g_R(t')|\psi_p(z,t-t')|^2 dt' \\ &+ i\xi_R\gamma\psi_p\int_{-\infty}^{\infty} g_R(t')\psi_p(z,t-t')\psi_s^*(z,t-t')e^{i\Omega_{sp}t'}dt',\end{aligned} \tag{57}$$

$$\begin{aligned}\frac{d\psi_s}{dz} &= -\Delta\frac{d\psi_s}{dt} - i\frac{\beta_{2_s}}{2}\frac{d^2\psi_s}{dt^2} + i\frac{\beta_{3_s}}{6}\frac{d^3\psi_s}{dt^3} - \frac{1}{2}[\alpha_s + \alpha_{FC_s}]\psi_s \\ &+ 2i\xi_e\left[\gamma + i\tfrac{1}{2}\beta_{TPA}\right]|\psi_p|^2\psi_s \\ &+ i\xi_R\gamma\psi_s\int_{-\infty}^{\infty} g_R(t')|\psi_p(z,t-t')|^2 dt' \\ &+ i\xi_R\gamma\psi_s\int_{-\infty}^{\infty} g_R(t')\psi_s(z,t-t')\psi_p^*(z,t-t')e^{-i\Omega_{sp}t'}dt'.\end{aligned} \tag{58}$$

A new quantity $\Delta = (\beta_{1s} - \beta_{1p})/2$ has been introduced in equations (57) and (58) in order to make sure that both the pump and probe pulses have the same distance from the centre of the calculation window.

4. Fabrication and optimization of single-mode silicon waveguides for all-optical processes

4.1. Fabrication

Single-mode operation of a SOI waveguide is preferred if one wishes to leverage third-order nonlinear effects because of the need for strong modal overlap and well-defined peak intensities. There are several methods to fabricate single-mode SOI waveguides (see section 4.5) of which a silicon wire waveguide with submicrometre cross sectional dimensions is the most attractive. For the fabrication of these waveguides state-of-the-art fabrication techniques are needed for the definition of the waveguide geometry, like deep UV lithography in combination with mask steppers [94], e-beam lithography (EBL) [95], nano-imprint lithography (NIL) [96, 97] and focused ion beam (FIB) etching [98–100], also known as ion milling.

Before reactive ion etching, electron cyclotron resonance etching [101] or wet chemical etching the pattern is often transferred into a silicon oxide hardmask to protect the underlying silicon. FIB can also be applied to directly pattern the silicon surface. The implantation, however, of gallium ions will cause additional losses due to the resulting crystal damage and free carriers. A protective layer of Al_2O_3 can drastically reduce the propagation losses of FIB fabricated structures [98]. For waveguides with larger dimensions, typically larger than $1\,\mu$m, standard UV lithography can be used in combination with reactive ion etching [102, 103]. References on how to keep large cross sectional rib waveguides in single-mode operation are given in section 4.5. An alternative method for the fabrication of single-mode SOI waveguides is to inscribe crystalline silicon using femtosecond laser pulses ($\lambda = 2.4\,\mu$m). This approach yields graded index waveguides with modal diameters ranging from 10–20 μm having losses as low as 0.7 dB cm^{-1} at 1550 nm [104].

Table 3 shows an overview of examples of several components and devices that have been realized in silicon and SOI using different fabrication methods.

To obtain high-quality waveguides, most devices are fabricated using SOI wafers as a starting material. However, a low-cost solution to obtain the silicon core material is to deposit hydrogenated amorphous silicon (a-Si:H) using plasma enhanced chemical vapour deposition (PECVD) instead of using expensive SOI wafers. Harke *et al* [139] reported losses of 0.5 dB cm^{-1} at 1550 nm for multimode waveguides and 2.0 dB cm^{-1} for single-mode a-Si : H waveguides fabricated using standard photo-lithography and dry etching with alternating SF_6 and O_2 gases and C_2F_8 for sidewall passivation. It should be noted, however, that the single-mode rib waveguides did not have submicrometre dimensions and therefore the propagation losses are most likely caused by the material absorption and material structure. That is, significant losses are not likely to come from sidewall roughness and substrate leakage, as is the case with submicrometre shaped waveguide cross sections (section 4.2). The rib waveguides were designed such that they showed single-mode operation (see section 4.5).

In principle, every conventional type of integrated optical component can be realized in silicon, either through standard lithography or state-of-the-art high-resolution methods, using amorphous, polycrystalline or single crystalline silicon, depending on the application. As a guideline, it can be concluded that most devices having multimode propagation regions, such as star couplers, MMIs and straight waveguides can easily be engineered such that standard lithography offers sufficient resolution. However, when small footprints, accurately shaped spotsize converters and evanescent coupling

Table 3. Overview of silicon components and devices realized with different fabrication methods.

Device	Technology	References
Straight, wires	EBL	[101]
Straight, wires	DUV	[94, 105]
Straight, rib	Standard lithography	[103]
Straight, graded index	Fs-writing	[104]
Beam splitter	Standard lithography	[106, 107]
Polarizing beam splitter	Standard lithography	[108]
Start coupler (1 × 2)		[109]
Start coupler (39 × 39)	Standard lithography	[110]
MMI (2 × 2)	Standard lithography	[111]
MMI (1 × 8)		[112]
Switch matrix (2 × 2)	Standard lithography and ion implantation	[44]
Switch matrix (2 × 2)	Standard lithography	[113, 114]
Switch matrix (4 × 4)	Standard lithography	[111, 115]
Switch matrix (8 × 8)	Standard lithography	[116]
Photonic bus	Standard lithography	[117]
Phased arrays	EBL and ion implantation	[118]
Phased arrays	Standard lithography	[119, 120]
Turning mirrors	Standard lithography	[111, 120]
Turning mirrors	UV contact	[102]
Turning mirrors	EBL	[121]
Turning mirrors	Dry and wet etching	[122]
Turning mirrors		[123]
Photonic crystals	EBL	[124]
Photonic crystals	193 nm DUV/stepper	[125]
Photonic crystals	248 nm DUV/stepper	[105]
Photonic crystals	Soft UV NIL	[97, 126]
Photonic crystals	FIB	[100]
Trenches	FIB	[99]
Microring resonators	Standard lithography	[127]
Microring resonators	248 nm DUV/stepper	[49, 94, 105]
Microring resonators	EBL	[95, 101, 128]
Microring resonators +(air suspended)	EBL	[129]
Microdisks MEMS	Standard lithography	[130]
Microdisks (buried)	SIMOX 3D sculpting	[131, 132]
Microdisks (p-i-n)		[133]
Racetrack resonators	Standard lithography	[134]
Racetrack resonators	EBL	[135]
Multiple racetracks		[136]
Bragg gratings	FIB	[137]
Grating couplers	FIB	[98]
Grating couplers	248 nm DUV/stepper	[105]
Grating couplers		[123]
Spotsize converters	193 nm DUV	[138]
Spotsize converters	Standard lithography	[114]
Spotsize converters	UV contact	[102]
Spotsize converters	EBL	[128]

between port waveguides and resonator structures are needed, standard lithography is not suitable anymore and the previously mentioned submicrometre fabrication methods, like deep UV lithography, EBL, NIL and FIB are needed.

4.2. Reduction of propagation losses

The strengths of the third-order nonlinear effects scale with the intensity of the optical signals in the waveguide, as discussed in section 2. It is therefore beneficial to keep the propagation losses in the waveguide as low as possible in order to effectively benefit from the nonlinearities. With this in mind we note that the losses in SOI wire waveguides are primarily dominated by the substrate leakage and scattering losses induced by the sidewall roughness of the waveguides. With small waveguide cross sections, the evanescent field of the mode will increase to dimensions that exceed the underlying buffer oxide, leading to substrate leakage [140]. A proper buffer thickness is therefore crucial for SOI waveguides with submicrometre dimensions. Furthermore, as the waveguide cross section decreases, the fraction of the light which interacts with the sidewall roughness increases. This leads to increased scattering. The scattering losses α_{sc} are also related to the refractive index contrast Δn between the SOI waveguide and the cladding material, the RMS value of the roughness σ and the normalized field intensity at the waveguide interface and may be determined according to Tien [141] by

$$\alpha_{sc} = \frac{\sigma 2k_0^2 n_{SOI}}{n_{eff}} \cdot \frac{E_S^2}{\iint E(x,y)^2 \mathrm{d}x\mathrm{d}y} \cdot \Delta n^2, \qquad (59)$$

where k_0 is the free-space wave number, n_{SOI} is the refractive index of bulk silicon, n_{eff} is the effective refractive index of the mode, E_S is the field intensity at the waveguide surface and $E(x,y)$ is the two-dimensional field profile. Several other models have been reported to calculate the scattering induced by sidewall roughness, such as the model proposed by Grillot *et al* [140] and the methods proposed by Lee [142], Marcuse [143] and Payne [144]. E-beam lithography typically yields SOI waveguides with lower losses compared with standard UV lithography. Vlasov *et al* [145] reported propagation losses of 3.6 dB cm^{-1} using a SiO_2 hardmask defined with e-beam lithography and HBr dry etching chemistry to pattern the SOI. There are several methods, however, to reduce the sidewall roughness when the fabrication process results in waveguides with unacceptable scattering losses. An efficient and straightforward method is thermal oxidation of the SOI waveguide and subsequent removal of the oxide using a HF wet etch step. A loss reduction from 32 to 0.8 dB cm^{-1} has been demonstrated this way for a waveguide with a cross section of 200 nm × 500 nm ($h \times w$) fabricated using G-line (436 nm) stepper lithography, indicating a roughness reduction from 10 to 2 nm [146]. A similar procedure using wet oxidation chemistries yielded a loss reduction from 9.2 to 1.9 dB cm^{-1} for waveguides fabricated using 248 nm stepper lithography [147]. An alternative method is to make use of the crystallographic orientation of the silicon and use a wet anisotropic etchant (25% NH_4OH at 80 °C) in combination with a SiO_2 hard mask [146]. One of the drawbacks of this method is that it only works for waveguides that are aligned with respect to the ⟨1 1 0⟩ crystal direction. Another drawback is that this method results in angled waveguide edges, which can cause a considerable amount of polarization conversion (see section 4.5). A dramatic sidewall roughness reduction from 20 to 0.26 nm has recently been reported by Lee *et al* [130, 148] by using 5 min annealing steps in a hydrogen environment at temperatures around 1100 °C. This method yields submicrometre rounded structures due to silicon atom migration. If the quality of the lithography process is too poor, the photoresist can be smoothened after photoresist development by thermal reflowing before the dry etching of the SiO_2 hardmask. Borselli *et al* [149] reported propagation losses as low as 0.1 dB cm^{-1} in silicon microdisks that were fabricated this way.

In addition to losses caused by substrate leakage and surface roughness, additional losses are caused by FCA, which

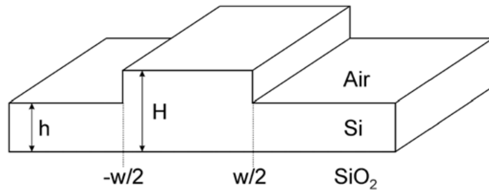

Figure 14. Schematic representation of a rib waveguide.

is often a problem when working with the intense optical fields that are typically needed for third-order nonlinear processes. From equations (7) and (8) it can be seen that the free-carrier density N is proportional to the free-carrier lifetime τ. This lifetime depends strongly on the method used for fabrication of the SOI wafer [24] and the waveguide geometry [38]. The free-carrier diffusion away from the waveguide mode area and recombination at the waveguide surface are the dominant effective lifetime reducing mechanisms in SOI waveguides.

Dimitropoulos *et al* [150] derived an analytical expression to predict the effective free-carrier lifetime τ_{eff} as function of the waveguide geometry for rib waveguides (figure 14):

$$\frac{1}{\tau_{\mathrm{eff}}} = \frac{1}{\tau_{\mathrm{b}}} + \frac{S}{H} + \frac{w+2(H-h)}{wH} S' + 2\frac{h}{H}\sqrt{\frac{D}{w^2}\left(\frac{1}{\tau_{\mathrm{b}}} + \frac{S+S'}{h}\right)}, \tag{60}$$

where τ_{b} is the bulk carrier recombination lifetime in silicon, S and S' are the interface and surface recombination velocities, D is the ambipolar diffusion coefficient, w accounts for the waveguide rib width, h represents the slab height and H includes the total rib height [35]. The effective lifetime is composed of the four terms in equation (60), i.e. the bulk recombination, the interface recombination, surface recombination and the diffusion of the free carriers away from the rib waveguide, respectively. In general, the interface recombination is the dominant mechanism and therefore the total rib height H has a strong influence on the effective lifetime, together with the interface recombination velocity S, which is dependent on the carrier density [151].

From equation (60) it follows that the lifetime can be reduced by decreasing the dimensions of the waveguide cross section. However, losses due to substrate leakage and surface scattering can increase as the waveguide cross section decreases. Another method to reduce the free-carrier lifetime is to induce recombination centres inside the waveguide, for instance by ion implantation. A free-carrier lifetime reduction from 100 to 1.9 ns has recently been demonstrated using helium implantation of silicon waveguides [152]. In this case, the recombination occurs primarily at recombination centres introduced inside the waveguide instead of at the waveguide interfaces. Free-carrier lifetime reduction after oxygen implantation resulted in relaxation times of 1.4 ps in silicon-on-sapphire (SOS) and 0.58 ps in amorphous silicon [153]. It should be noted however, that the implantation damage can result in high propagation losses, as noted by Knights *et al* [154] who measured a linear dependence of the optical loss in dB cm^{-1} as a function of the Si-ion implantation dose experimentally. Nevertheless, it is worth pointing out that the induced losses could be significantly reduced by thermal annealing.

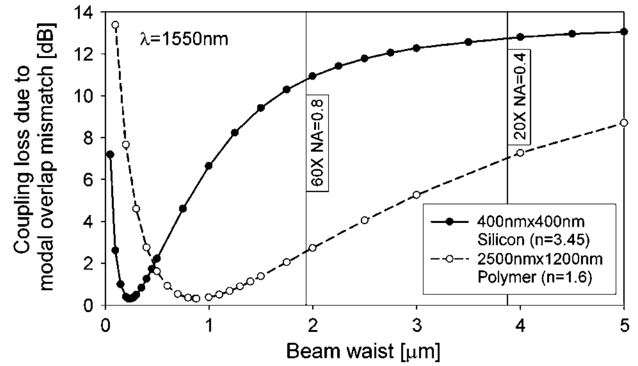

Figure 15. Coupling losses due to modal overlap mismatch for high- and moderate-contrast waveguides. Vertical lines indicate the beam waist at the focus point for different microscope objectives.

4.3. Improvement of the coupling efficiency

The coupling losses from free space or an optical fibre to a silicon photonic chip are large because of the small cross sectional dimensions of silicon wire waveguides. Specifically, the coupling losses are caused by the modal overlap mismatch between the fibre and waveguide mode, a mismatch in the numerical apertures and Fresnel reflections. Figure 15 shows the coupling losses due to the modal mismatch, calculated with a finite-difference based modesolver [155], for a high SOI contrast waveguide and relatively low contrast polymer waveguide. It can be concluded that the losses are minimal when the beam waist in the focal plane of the microscope objective matches the mode size of the waveguide. For most practical applications, however, the numerical aperture of the microscope objective used does not exceed 0.8; this limits the minimum beam waist to ~1.9 μm at 1550 nm. This size beam waist is much too large for high-index contrast single-mode waveguides, which typically have a mode size ranging from a few hundred nanometres up to 1 μm. Figure 15 shows that the modal overlap mismatch losses are >10 dB per facet for a silicon waveguide with submicrometre dimensions.

In order to enhance the coupling efficiency, several methods can be applied, both on the chip itself or externally. Among the methods that have been suggested and reported in the literature we mention the covering of the SOI waveguide with a graded index layer stack [156, 157] or a step-index top layer [157] to create a larger input facet, resulting in a larger modal size at the input facet. One-dimensional tapering [158, 159], two-dimensional tapering with [160] and without a polymer top cladding [161] and bi-level tapering [102, 162] have been used as spotsize converters. Out-of-plane micro-mirrors [163], slanted gratings [164] and standard gratings can be applied to couple perpendicular from free space [98, 165] with high alignment tolerance. The coupling efficiency of the gratings can be further increased using top and bottom mirrors [166]. Other examples of on-chip structures for efficient coupling are directional couplers [167] and non-periodic waveguide sections of which the dimensions have been optimized using genetic optimization algorithms [168, 169]. Optimization outside the chip is also possible through specially constructed fibre tips fabricated with a photo polymerization technique [170] or commercially available tapered and/or lensed fibre tips.

4.4. Dispersion management

The higher-order dispersion terms depend on both waveguide dimensions and material dispersion. The latter can be derived from the wavelength dependent refractive index $n(\lambda)$, which may be approximated by either the Sellmeier, Hartmann or Cauchy formulas. The latter type has the form

$$n(\lambda) = A + \frac{B}{(10^6\lambda)^2}, \tag{61}$$

where A and B are the Cauchy fitting parameters and λ the wavelength (in nm). Since the NLSE (see section 3.2) describes the propagation of optical fields in time and space, it is convenient to express $n(\lambda)$ in terms of frequency. The frequency dependent refractive index $n(\omega)$ can simply be expressed as follows:

$$n(\omega) = A + \frac{B}{(10^6 \times 2\pi(c/\omega))^2}, \tag{62}$$

since $\omega = 2\pi c/\lambda$ in radians s^{-1}. Now, a frequency dependent propagation constant can be defined:

$$\beta(\omega) = n(\omega)\frac{\omega}{c}. \tag{63}$$

By performing a Taylor-series expansion of $\beta(\omega)$ around a centre frequency ω_0, we obtain an expression which facilitates analytical and numerical investigations

$$\beta(\omega) = \beta_0 + \beta_1(\omega - \omega_0) + \tfrac{1}{2}\beta_2(\omega - \omega_0)^2 + \tfrac{1}{6}\beta_3(\omega - \omega_0)^3 + \tfrac{1}{24}\beta_4(\omega - \omega_0)^4 + \cdots. \tag{64}$$

The β_j components in the expansion above describe the various different physical effects governing the propagation of a pulse through a medium. The first term β_0 is related to the phase velocity, according to

$$\beta_0 = \frac{\omega_0}{v_\phi} = \frac{2\pi n_{\text{eff}}}{\lambda}. \tag{65}$$

The second term β_1, commonly referred to as the reciprocal group velocity, describes the group delay and is inversely proportional to the velocity v_g of the pulse envelope via

$$\beta_1 = \frac{d\beta}{d\omega} = \frac{1}{c}\left(n + \omega\frac{dn}{d\omega}\right) = \frac{1}{c}\left(n - \lambda\frac{dn}{d\lambda}\right) = \frac{1}{v_g}. \tag{66}$$

The group velocity dispersion (GVD) which causes symmetric pulse broadening is represented by β_2 and can be written as

$$\beta_2 = \frac{d\beta_1}{d\omega} = \frac{1}{c}\left(2\frac{dn}{d\omega} + \omega\frac{d^2n}{d\omega^2}\right). \tag{67}$$

At a wavelength where β_2 equals zero there will be no change to the temporal field envelope; consequently this wavelength is called the 'zero-dispersion wavelength'. For practical reasons we point out that the frequently used dispersion parameter D (expressed in ps (km × nm)$^{-1}$) is related to β_2 via [171]

$$D = \frac{d\beta_1}{d\lambda} = -\frac{2\pi c}{\lambda^2}\beta_2. \tag{68}$$

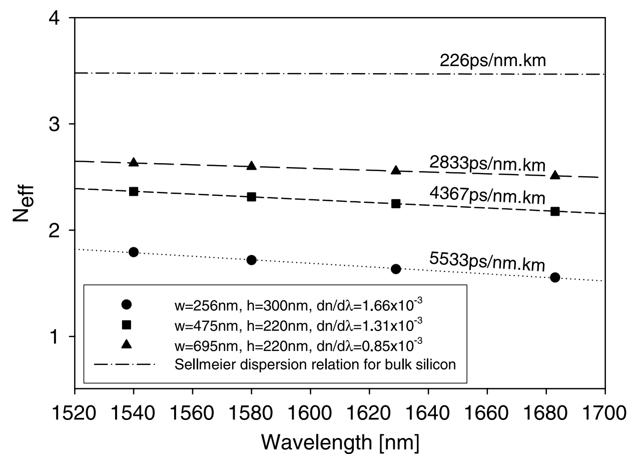

Figure 16. Dispersion of bulk silicon and some silicon waveguides with different cross sections etched in a SOI substrate.

When working with ultrashort high-power laser pulses, the third-order dispersion (TOD, related to dispersion slope S) and in some cases even fourth-order dispersion (FOD), terms become significant and need to be taken into account. Here we simply note that the TOD term is given by

$$\beta_3 = \frac{d\beta_2}{d\omega} = \frac{1}{c}\left(3\frac{d^2n}{d\omega^2} + \omega\frac{d^3n}{d\omega^3}\right) \tag{69}$$

and the fourth-order term can be obtained by taking the derivative of β_3.

Dispersion is always an important issue when working with short pulses or nonlinear mechanisms which require phase matching, however, even in pump–probe experiments, where the pump and probe pulses can have large wavelength separations (for instance ~135 nm for Raman gain), dispersion becomes important. Figure 16 shows the dispersion of bulk silicon (measured material dispersion) and the simulated dispersion for various SOI waveguide geometries. It can be concluded that the waveguide dispersion is about one order of magnitude higher than the material dispersion. Dulkeith *et al* [172] reported similar GVD values of 4400 ps (nm × km)$^{-1}$ at 1550 nm, being almost three orders of magnitude higher than in standard silica fibres.

The effective indices of the waveguides have been determined using a fully-vectorial finite-difference method (Olympios from C2V [155]). The extremely strong dispersion effects cause a strong walk-off between pump and probe pulses. For instance, assume that pump and probe pulses arrive at the silicon waveguide input facet with zero time delay. The probe pulse will propagate faster and exits a 7-mm waveguide about 7 ps earlier than the pump pulse. The average propagation time is about 60 ps. This means that the pulses ($T_0 \sim 300$ fs) overlap only as they propagate through a fraction of the waveguide.

Tsang *et al* [173] studied the first-order dispersion of a 4 μm wide rib waveguide using 54 ps pulses. They found that the dispersion was only −910 ps (nm × km)$^{-1}$. However, when the SOI waveguide dimensions are in the submicrometre range, the geometry-induced waveguide dispersion will dominate the material dispersion [93], which can be concluded from figure 16. It is therefore of great importance to understand the dispersion characteristics of SOI nanowires when a large

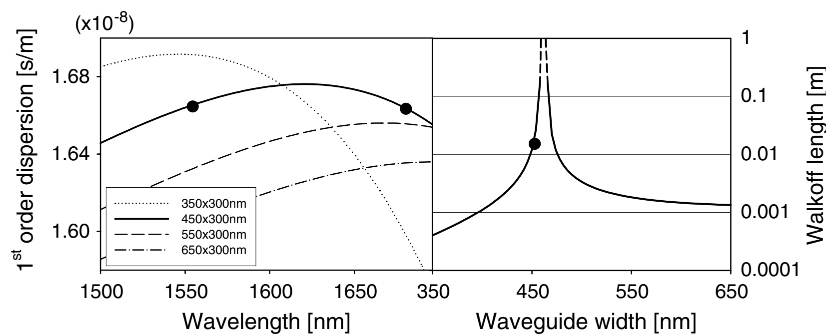

Figure 17. Left: first-order dispersion as a function of wavelength. Pump and probe wavelengths are marked with black dots. Right: walk-off length as a function of waveguide width. The waveguide width of the waveguide used in the experiments is marked with a black dot [23].

interaction between pump and probe pulses is desirable, i.e. when one seeks to use XPM and/or FWM in experiments. The characteristic walk-off length L_w represents the distance over which the pump and probe pulses pass through each other's envelope [93] and is given by

$$L_w(\lambda) = T_0/|\beta_{1p}(\lambda) - \beta_{1s}(\lambda)|, \qquad (70)$$

where T_0 is the width of the pulse (at $1/e$ intensity), and $\beta_{1p}(\lambda)$ and $\beta_{1s}(\lambda)$ are the first-order dispersion coefficients of the pump and probe wavelengths, respectively. The XPM induced wavelength conversion, for instance, scales with the walk-off length, according to (35). In figure 17 the first-order dispersion coefficients and walk-off lengths between 1554 nm pump and 1683 nm probe pulses are plotted for a SOI waveguide with a height of 300 nm while the width of the waveguide is varied. The effective mode indices needed for the determination of the dispersion coefficients were obtained with the aid of a vectorial finite-difference based mode solver [174] taking the silicon material dispersion into account [175]. It can be seen that the waveguide width is a critical parameter that strongly affects the pump–probe interaction and therefore the maximum attainable wavelength conversion as the conversion efficiency increases with L_w. Focusing on Raman amplification we point out that the dispersion is less critical, since the lifetime of the optical phonons in silicon is in the order of 3 ps [77] facilitating a temporal overlap of the phonon lifetimes and the probe pulses up to delay times of a few picoseconds. Although the Raman effect is nearly two orders of magnitude stronger than the Kerr effect in silicon, for subpicosecond pulses, the pump pulses are too short to efficiently excite Raman phonons [24]. The Raman effect is suppressed as long as the pulse length is less than the phonon de-phasing time, which is in the order of 10 ps [176]. Since the walk-off length scales linearly with the pulse length according to equation (70), it can be concluded that the interaction length can easily be increased by increasing the pulse lengths. However, at longer pulse lengths the pulse envelope is less steep resulting in weaker XPM-induced wavelength conversion.

The dots in the left graph of figure 17 indicate the pump and probe wavelengths used in our experiments, respectively. The dot in the right graph marks the walk-off length between pump and probe pulses in 450 nm × 300 nm SOI waveguides. In principle, a SOI waveguide can be designed such that there is no walk-off for a given set of wavelengths; however, nanometre fabrication precision would be needed to achieve this. It would be easier to choose the pump and probe wavelengths such that they show equal reciprocal group velocity, i.e. $\beta_p = \beta_s$.

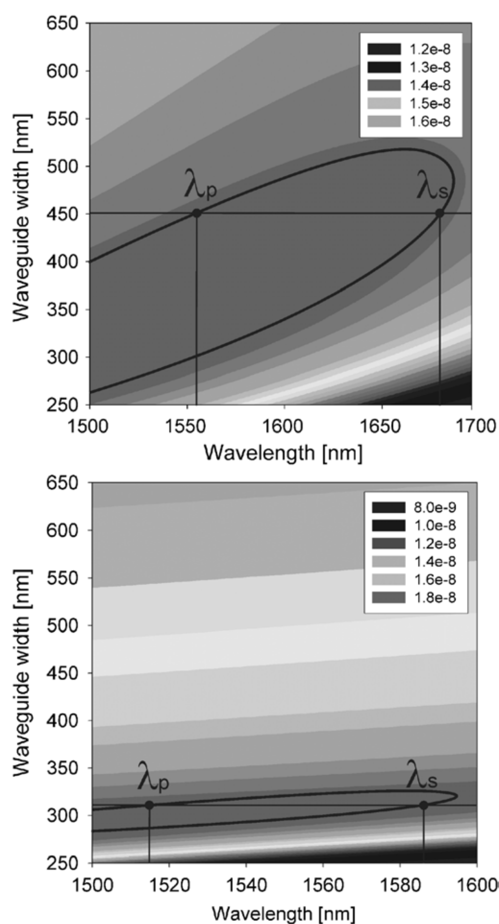

Figure 18. First-order dispersion coefficients β_1 for TM (top) and TE (down) polarized light as a function of waveguide width and wavelength for a SOI waveguide with a height of 300 nm.

To illustrate the influence of the waveguide geometry on the first-order dispersion coefficients in greater detail we displayed the simulation results already used in figure 17 using a surface plot. Figure 18 shows the first-order dispersion coefficients for both TM and TE polarization for a SOI waveguide with a thickness of 300 nm. The black curves

represent examples of equal dispersion values. It is possible to achieve efficient interaction between pump and probe pulses for waveguide widths where the horizontal line crosses such an iso-dispersion line twice, i.e. when the difference between the group velocities is small. The pump and probe wavelengths, λ_p and λ_s, should be chosen such that they match the intersection between waveguide width and an iso-dispersion line. It can be concluded from figure 18 that there is only a small range of suitable waveguide widths for TE polarized light for a waveguide thickness of 300 nm.

Dispersion tailoring is a good solution when the wavelength tunability of the sources is limited. Yin *et al* [177] theoretically showed that the zero-dispersion wavelength (ZDW) can be shifted from 2 μm down to 1.5 μm using dispersion tailoring, enabling solitons-like propagation of 130 fs pulses. Hsieh *et al* [68] observed soliton-emitted radiation in their SOI wire waveguides with a TOD of $\beta_3 = -0.73\,\text{ps}^3\,\text{m}^{-1}$ using 200 fs pulses with a 1537 nm centre wavelength. Turner *et al* [178] were able to experimentally tune the GVD from -2000 to 1000 ps $(\text{nm}\times\text{km})^{-1}$ by tailoring the waveguide cross section. A 34% decrease of the dispersion at 1450 nm is predicted theoretically by Lou *et al* [179] via a slight diameter reduction of 1% of a circular silicon wire through oxidation of the waveguide surface.

Phase matching is extremely important for FWM, as previously discussed in section 2.4.4. FWM conversion efficiencies of tens of percents are predicted in a 2 cm phase-matched SOI waveguide by Dimitropoulos *et al* [180] who states that such high efficiencies can only be achieved if the waveguide cross section is accurately controlled.

4.5. Polarization dispersion

The waveguide cross section of SOI waveguides can be designed such that the polarization dispersion is minimized. This can, for instance, be achieved by modelling the etch depth of a rib waveguide such that the effective indices of the TE and TM modes become equal [181]. This method has been applied by Headley *et al* [182] for the design of a polarization independent racetrack resonator. The length of the coupling region was varied until a length was found where total power transfer of the optical field was achieved for both polarizations. Caution should be paid to the minimum bend radius of the rib waveguide, since the TE mode shows significantly larger bend losses compared with the TM mode [183].

In a SOI wire waveguide, polarization independence is typically found only when the waveguide cross section has a height and width that are approximately equal. Figure 19 shows the effective refractive indices of SOI wire waveguides in air at a wavelength of 1550 nm for both TE and TM polarization as a function of waveguide width where the height of the waveguide is once again 300 nm. It can be seen that both the curves of the effective indices cross at a thickness of 315 nm. The reason polarization independence is obtained at 315 nm instead of 300 nm can be explained by the fact that the refractive indices of the SiO_2 buffer and air cladding are not matched.

Which type of waveguide should be chosen, i.e. rib waveguide or wire waveguide, depends on the application. Reed *et al* [184] recently presented an extensive overview

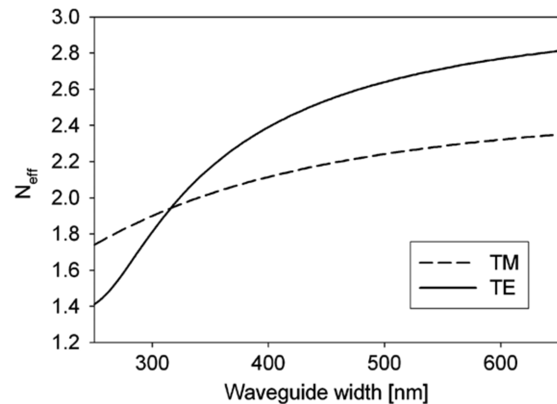

Figure 19. Calculated effective refractive indices for a wavelength of 1550 nm in SOI waveguides with a thickness of 300 nm as a function of waveguide width.

on the polarization issues in SOI waveguides which examines some of these issues in further detail.

An alternative method for polarization or birefringence control is stress engineering of SOI waveguides by applying a stress-inducing SiO_2 top cladding on rib waveguides with slanted and straight sidewalls [185]. This method has been applied for the design of polarization insensitive microring resonators using MMI couplers [186].

When operation with a single polarization is required, polarization filters can be applied for example with 20.3 dB extinction ratio for TE at 1550 nm by applying a subwavelength wide slot at the centre of the waveguide [187].

Polarization conversion in high index-contrast waveguides can effectively be enhanced by stress and structural deformations of the waveguide [188]. Brooks *et al* [189] reported 75% polarization conversion efficiency in their experiments using asymmetric waveguides with both a straight and slanted sidewall. The performance was limited due to fabrication errors. Deng *et al* [190] reported design rules for such slanted angle polarization converters and predicted conversion efficiencies of 99.98%.

Moreover, optical isolators can be fabricated in SOI by combining the slotted waveguide-based polarization filter [187] with slanted angle polarization rotators.

4.6. Waveguide cross section

As we have already discussed (in section 4.1), single-mode operation of a SOI waveguide is beneficial if one wishes to leverage third-order nonlinear effects in pump–probe experiments, because the modal overlap between pump and probe signals is higher and the peak intensity of the fundamental mode is larger than that of the higher-order mode.

In 1991, Soref *et al* [191] derived design rules for single-mode operation of silicon on silica rib waveguides with dimensions that would intuitively result in multimode operation. Others have studied the single-mode conditions of rib waveguides with 90° sidewall angles [192] as well as slanted angle and trapezoidal shaped waveguides [193, 194]. Chan *et al* [195] presented an overview of the work that has been reported for the design of large single-mode rib waveguides. However, all these methods are limited to

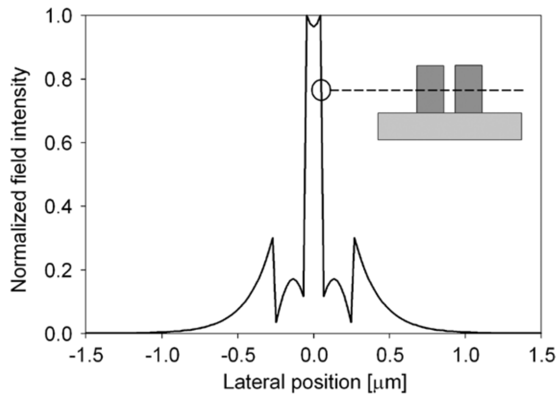

Figure 20. Normalized field intensity along the lateral direction of a slot silicon wire waveguide with a width of 500 nm and a slot of 100 nm. The inset shows a schematic cross section of the slot waveguide on a silica buffer and an air cladding.

shallowly etched rib waveguides where the ratio between the etch depth and the thickness of the waveguide is larger than 0.5. Chan *et al* [195] also proposed approximate design rules for the single-mode and polarization independent operation of deeply etched small SOI waveguides.

Since the peak intensity is inversely proportional to the waveguide cross section, it is logical to choose SOI wire waveguides with submicrometre dimensions. Unfortunately, these waveguides can only be fabricated using state-of-the-art processing methods like EBL, NIL FIB and DUV processes.

In figure 19 the effective refractive indices for the fundamental TE and TM mode for a waveguide with 300 nm thickness as a function of wire width are shown. However, at large wire widths (typically >500 nm) the silicon wire waveguide becomes multimode. An extensive study of the single-mode conditions for silicon and silica wires has been reported by Tong *et al* [196].

Optical field intensities can be even further enhanced by etching a slot in the centre of the silicon wire waveguide. When properly designed, the field will be strongly confined in the etched slot instead of being located in the higher index silicon material [197]. Figure 20 shows an example of the normalized field distribution of a silicon slot waveguide. Xu *et al* [198] have already experimentally demonstrated this effect in silicon waveguides. A 30% reduction in the effective index confirmed that the guiding took place in the low index material. Waveguide slots can also be applied in microring resonators [198] and bends. Anderson *et al* [199] presented an analysis of the optical properties as a function of the lateral position of the slot and found that 28% of the power is located in the air slot for bend radii as low as 1 μm for an optimized asymmetric slot-based bend. High-Q slotted optical ring resonators have also been experimentally demonstrated, showing promising properties for sensing and nonlinear optics [200]. For applications in nonlinear optics, the slot can be filled with materials having a Kerr nonlinearity which is higher than that of silicon to enhance the nonlinear response of the resonator. For example, filling of the slot with silicon nanocrystal-doped silica (Si-nc:SiO_2) has been proposed. The switching time of such resonators is enhanced in this way such that they compete well with high-performance III–V based all-optical microring switches [201]. Another benefit of slot waveguides is the fact that fewer free carriers will be generated in the silicon, which could substantially enhance the switching speed and reduce the roundtrip losses.

In addition to straight waveguides, bends and microring resonators, a polarization independent directional coupler based on slot waveguides has been suggested by Fujisawa *et al* [202]

5. Conclusion

We have presented an extensive overview of recent results that have been obtained in the field of ultrafast third-order nonlinear SOI waveguide photonics. Nonlinear phenomena including TPA, FCA, SPM, XAM, XPM, FWM and SRS were introduced and explored. Two efficient modelling tools useful in predicting nonlinear pulse propagation in SOI nanowires have been explained in detail and the importance of waveguide cross section, waveguide dispersion and polarization properties for efficient nonlinear operation are discussed.

Acknowledgments

The authors would like to thank the Freeband Impulse technology programme of the Ministry of Economic Affairs of the Netherlands and acknowledge the European Network of Excellence on Photonic Integrated Components and Circuits (ePIXnet FAA5/WP11).

References

[1] Reed G T 2004 *Nature* **427** 595–6
[2] Web of Science, http://apps.isiknowledge.com/WoS
[3] Lipson M 2005 *J. Lightwave Technol.* **23** 4222–38
[4] Jalali B, Paniccia M and Reed G 2006 *IEEE Microw. Mag.* **6** 58–68
[5] Lipson M 2004 *Nanotechnology* **15** S622-7
[6] Lipson M 2005 *Opt. Mater.* **27** 731–9
[7] Dumon P *et al* 2006 *Japan J. Appl. Phys.* **45** 6589–602
[8] Soref R A 2006 *IEEE J. Sel. Top. Quantum Electron.* **12** 1678–87
[9] Hoang T, Phuong L, Holleman J and Schmitz J 2006 *IEEE Electron Device Lett.* **27** 105–7
[10] Huang Z, Carey J E, Liu M, Guo X, Mazur E and Campbell J C 2006 *Appl. Phys. Lett.* **89** 033506
[11] Bradley J D B, Jessop P E and Knights A P 2005 *Appl. Phys. Lett.* **86** 241103
[12] Knights A P, Bradley J D B, Gou S H and Jessop P E 2006 *J. Vac. Sci. Technol.* A **24** 783–6
[13] Colace L, Masini G, Altieri A and Assanto G 2006 *IEEE Photon. Technol. Lett.* **18** 1094–6
[14] Colace L, Balbi M, Masini G and Assanto G 2006 *Appl. Phys. Lett.* **88** 101111
[15] Masini G, Cencelli V, Colace L, Notaristefani F D and Assanto G 2004 *IEEE J. Sel. Top. Quantum Electron.* **10** 811–15
[16] Raghunathan V, Claps R, Dimitropoulos D and Jalali B 2005 *J. Lightwave Technol.* **23** 2094–102
[17] Liu A, Rong H, Paniccia M, Cohen O and Hak D 2004 *Opt. Express* **12** 4261–8
[18] Xu Q, Almeida V R and Lipson M 2004 *Opt. Express* **12** 4437–42
[19] Liang T K, Tsang H K, Day I E, Drake J, Knights A P and Asghari M 2002 *Appl. Phys. Lett.* **84** 2745–7
[20] Boyraz O, Indukuri T and Jalali B 2004 *Opt. Express* **12** 829–34

[21] Dekker R, Klein E J, Niehusmann J, Först M, Ondracek F, Ctyroky J, Usechak N and Driessen A 2005 *Symp. IEEE/LEOS Benelux Chapter (Mons, Belgium)* p 197–200
[22] Dulkeith E, Vlasov Y A, Chen X, Panoiu N C and Osgood R M Jr 2006 *Opt. Express* **14** 5524–34
[23] Dekker R, Wahlbrink T, Moormann C, Niehusmann J, Först M and Driessen A 2006 *Opt. Express* **14** 8336–46
[24] Boyraz O, Koonath P, Raghunathan V and Jalali B 2004 *Opt. Express* **12** 4094–102
[25] Fukuda H, Yamada K, Shoji T, Takahashi M, Tsuchizawa T, Watanabe T, Takahashi J and Itabashi S 2005 *Opt. Express* **13** 4629–37
[26] Dinu M, Quochi F and Garcia H 2003 *Appl. Phys. Lett.* **82** 2954–6
[27] Hase M, Kitajima M, Constantinescu A M and Petek H 2006 *Nature* **426** 51–4
[28] Notomi M, Taniyama H, Mitsugi S and Kuramochi E 2006 *Phys. Rev. Lett.* **97** 023903–01
[29] Sharping J E, Lee K F, Foster M A, Turner A C, Schmidt B S, Lipson M, Gaeta A L and Kumar P 2006 *Opt. Express* **14** 12388–93
[30] Reed G T and Jason C E 2005 *Mater. Today* **1** 40–50
[31] Jacobsen R S *et al* 2006 *Nature* **441** 199–202
[32] Liang T K *et al* 1995 *Opt. Express* **13** 7298–03
[33] Rauscher C and Laenen R 1997 *J. Appl. Phys.* **81** 2818–21
[34] Jones R, Rong H, Liu A, Fang A W, Paniccia M J, Hak D and Cohen O 2005 *Opt. Express* **13** 519–25
[35] Jalali B, Raghunathan V, Dimitropoulos D and Boyraz Ö 2006 *IEEE J. Sel. Top. Quantum Electron.* **12** 412–21
[36] Liang T K and Tsang H K 2004 *IEEE J. Sel. Top. Quantum Electron.* **10** 1149–53
[37] Rong H, Liu A, Nicolaescu R, Paniccia M, Cohen O and Hak D 2004 *Appl. Phys. Lett.* **85** 2196–8
[38] Claps R, Raghunathan V, Dimitropoulos D and Jalali B 2004 *Opt. Express* **12** 2774–80
[39] Priem G, Bienstman P, Morthier G and Baets R 2006 *J. Appl. Phys.* **99** 063103
[40] Soref R A and Bennett B R 1987 *IEEE J. Sel. Top. Quantum Electron.* **23** 123–9
[41] Cowan A R, Rieger G W and Young J F 2004 *Opt. Express* **12** 1611–21
[42] Preble S F, Xu Q, Schmidt B S and Lipson M 2005 *Opt. Lett.* **30** 2891–3
[43] Lipson M 2006 *IEEE J. Sel. Top. Quantum Electron.* **12** 1520–6
[44] Fei S, Jin-Zhong Y and Shao-Wu C 2005 *Chin. Phys. Lett.* **22** 3097–9
[45] Xu Q, Almeida V R and Lipson M 2005 *Opt. Lett.* **30** 2733–5
[46] Almeida V R, Barrios C A, Panepucci R R and Lipson M 2004 *Nature* **431** 1081–4
[47] Manolatou C and Lipson M 2006 *J. Lightwave Technol.* **24** 1433–9
[48] Xu Q and Lipson M 2006 *Opt. Lett.* **31** 341–3
[49] Priem G, Dumon P, Bogaerts W, Thourhout D V, Morthier G and Baets R 2006 *Opt. Express* **13** 9623–8
[50] Johnson T J, Borselli M and Painter O 2006 *Opt. Express* **14** 817–31
[51] Ndi F C, Toulouse J, Hodson T and Prather D W 2006 *Opt. Express* **14** 4835–41
[52] Ndi F C, Toulouse J, Hodson T and Prather D W 2005 *Opt. Lett.* **30** 2254–6
[53] Barclay P E, Srinivasan K and Painter O 2005 *Opt. Express* **13** 801–20
[54] Uesugi T, Song B S, Asano T and Noda S 2005 *Opt. Express* **14** 377–86
[55] Gan F, Grawert F J, Schley J M, Akiyama S, Michel J, Wada K, Kimerling L C and Kärtner F X 2006 *J. Lightwave Technol.* **24** 3454–63
[56] Barrios C A and Lipson M 2006 *J. Lightwave Technol.* **24** 2898–905
[57] Bosshard C, Spreiter R, Zgonik M and Günter P 1995 *Phys. Rev. Lett.* **74** 2816–9
[58] Coso R D and Solis J 2004 *J. Opt. Soc. Am.* B **21** 640–4
[59] Samoc M, Samoc A, Luther-Davies B, Bao Z, Yu L, Hsieh B and Scherf U 1998 *J. Opt. Soc. Am.* B **15** 817–25
[60] DeSalvo R, Said A A, Hagan D J, Stryland E W V and Sheik-Bahae M 1996 *IEEE J. Quantum Electron.* **32** 1324–33
[61] Priem G, Notebaert I, Bienstman P, Morthier G and Baets R 2005 *J. Appl. Phys.* **97** 023104
[62] Vonsovici A and Koster A 1999 *J. Lightwave Technol.* **17** 129–35
[63] Rong H, Jones R, Liu A, Cohen O, Hak D, Fang A and Pannicia M 2005 *Nature* **433** 725–8
[64] Liang T K, Nunes L R, Tsuchiya M, Abedin K S, Miyazaki T, Thourhout D V, Bogaerts W, Dumon P, Baets R and Tsang H K 2006 *Opt. Commun.* **265** 171–4
[65] Cocorullo G and Rendina I 1992 *Electron. Lett.* **28** 83–5
[66] Ghosha G 1995 *Appl. Phys. Lett.* **66** 3570–2
[67] Baehr-Jones T, Hochberg M, Walker C, Chan E, Koshinz D, Krug W and Scherer A 2005 *J. Lightwave Technol.* **23** 4215–21
[68] Hsieh I W, Chen X, Dadap J I, Panoiu M C, Osgood R M Jr, McNab S J and Vlasov Y A 2006 *Opt. Express* **14** 12380–7
[69] Dekker R, Niehusmann J, Först M and Driessen A 2007 *Euro. Conf. on Integrated Optics ECIO (Copenhagen, Denmark)* Paper ThC1.
[70] Espinola R L, Dadap J I, Osgood R M Jr, Mc S JNab and Vlasov Y A 2005 *Opt. Express* **13** 4341–9
[71] Yamada K, Fukuda H, Tsuchizawa T, Watanabe T, Shoji T and Itabashi S 2006 *IEEE Photon. Technol. Lett.* **18** 1046–8
[72] Rong H, Kuo Y H, Liu A, Paniccia M and Cohen O 2006 *Opt. Express* **14** 1182–8
[73] Lin Q, Zhang J, Fauchet P M and Agrawal G P 2006 *Opt. Express* **14** 4786–99
[74] Foster M A, Turner A C, Sharping J E, Schmidt B S, Lipson M and Gaeta A L 2006 *Nature Lett.* **441** 960–3
[75] Lin Q and Agrawal G P 2006 *Opt. Lett.* **31** 3140–2
[76] Parker J H J, Feldman D W and Ashkin M 1967 *Phys. Rev.* **155** 712–4
[77] Xu Q, Almeida V R and Lipson M 2005 *Opt. Lett.* **30** 35–7
[78] Adu K W, Gutiérrez H R, Kim U J, Sumanasekera G U and Ecklund P C 2005 *Nano Lett.* **5** 409–14
[79] Sirleto L, Raghunatan V, Rossi A and Jalali B 2004 *Electron. Lett.* **40** 1221–2
[80] Niu J, Sha J, Wang L, Ji Y and Yang D 2005 *Physica* E **27** 309–13
[81] Iqbal Z and Veprek S 1982 *J. Phys.* C **15** 377–92
[82] Pivac B, Furic K, Desnica D, Borghesi A and Sassella A 1999 *J. Appl. Phys.* **86** 4383–6
[83] Liang T K and Tsang H K 2004 *Appl. Phys. Lett.* **85** 2745–7
[84] Rong H, Kuo Y H, Xu S, Ansheng L, Jones R, Paniccia M, Cohen O and Raday O 2006 *Opt. Express* **14** 6705–12
[85] Espinola R L, Dadap J I, Osood R M Jr, McNab S J and Vlasov Y A 2004 *Opt. Express* **12** 3713–8
[86] Dadap J I, Espinola R L, Osood R M Jr, McNab S J and Vlasov Y A 2004 *Opt. Lett.* **29** 2755–7
[87] Claps R, Dimitropoulos D, Raghunathan V, Han Y and Jalali B 2003 *Opt. Express* **11** 1731–9
[88] Agrawal G P 1995 *Nonlinear Fiber Optics, Optics and Photonics* (Toronto: Academic).
[89] Laniel J M, Hô N and Vallée R 2005 *J. Opt. Soc. Am.* B **22** 437–5
[90] Bandelow U, Demircan A and Kesting M 2003 Simulation of pulse propagation in nonlinear optical fibers *Report No* ISSN 0946–8838
[91] Blow K J and Wood D 1989 *IEEE J. Quantum. Electron.* **25** 2665–73
[92] HeadleyIII C and Agrawal G P 1996 *J. Opt. Soc. Am.* B **13** 2170–7

[93] Chen X, Panoiu N C and Osgood R M Jr 2006 *IEEE J. Quantum. Electron.* **42** 160–70
[94] Dumon P *et al* 2004 *IEEE Photon. Technol. Lett.* **16** 1328–30
[95] Niehusmann J, Vörckel A, Bolivar P H, Wahlbrink T, Henschel W and Kurz H 2004 *Opt. Lett.* **29** 2861–3
[96] Bender M, Plachetka U, Ran J, Fuchs A, Vratzov B, Kurz H, Glinsner T and Lindner F 2004 *J. Vac. Sci. Technol.* B **22** 3229–32
[97] Belotti M, Torres J, Roy E, Pépin A, Gerace D, Andreani L C and Galli M 2006 *J. Appl. Phys.* **99** 024309
[98] Schrauwen J, Thourhout D V and Baets R 2006 *Appl. Phys. Lett.* **89** 141102
[99] Lugstein A, Basnar B, Smoliner J and Bartagnolli E 2003 *Appl. Phys.* A **76** 545–548
[100] Hopman W C L, Ay F, Hu W, Gadgil V J, Kuipers L, Pollnau M and de Ridder R M 2007 *Nanotechnology* **18** 195305
[101] Tsuchiwaza T, Yamada K, Fukada H, Watanabe T, Takahashi J I, Takahashi M, Shoji T, Tamechika E, Itabashi S I and Morita H 2005 *IEEE J. Sel. Top. Quantum Electron.* **11** 232–40
[102] Solehmainen K, Aalto T, Dekker J, Kapulainen M, Harjanne M and Heimala P 2006 *J. Opt. A: Pure Appl. Opt.* **8** S455-60
[103] Solehmainen K, Aalto T, Dekker J, Kapulainen M, Harjanne M, Kukli K, Heimala P, Kolari K and Leskelä M 2005 *J. Lightwave Technol.* **23** 3875–80
[104] Nejadmalayeri A M, Herman P R, Burghoff J, Will M, Nolte S and Tünermann A 2005 *Opt. Lett.* **30** 964–6
[105] Bogaerts W, Tailleart D, Luyssaert B, Dumon P, Campenhout J V, Bienstman P, Thourhout D V, Baets R, Wiaux V and Beckx S 2004 *Opt. Express* **12** 1583–91
[106] Zhilang L, XinLi C, YongJin W, GongBai C, XioaLin J and Feng Z 2004 *Opt. Commun.* **240** 269–74
[107] Wang Y, Cheng X, Lin Z, Gao F and Zhang F 2004 *Opt. Express* **12** 5154–9
[108] Liang T K and Tsang H K 2005 *IEEE Photon. Technol. Lett.* **17** 393–5
[109] Koster A, Cassan E, Laval S, Vivien L and Pascal D 2004 *J. Opt. Soc. Am.* A **21** 2180–5
[110] Cao G B, Dai L J, Wang Y J, Jiang J, Yang H and Zhang F 2005 *IEEE Photon. Technol. Lett.* **17** 2616–8
[111] Liu J, Yu J, Chen S and Li Z 2005 *Opt. Eng.* **44** 070503
[112] Tang Y, Wang W, Wu Y, Yang J and Wang Y 2004 *Opt. Eng.* **43** 2495–6
[113] Liu J, Zu J, Chen S and Xia J 2005 *Opt. Commun.* **245** 137–44
[114] Yan-Ping L, Jin-Zhong Y and Shao-Wu C 2005 *Chin. Phys. Lett.* **22** 1449–51
[115] Yang D, Li Y, Sun F, Chen S and Yu J 2005 *Opt. Commun.* **250** 48–53
[116] Yan-Ping L, Di Y, Fei S, Shao-Wu C and Jin-Zhong Y 2005 *Chin. Phys. Lett.* **22** 621–3
[117] Hsu S and Chan J 2006 *Opt. Lett.* **31** 2142–4
[118] Lim S T, Png C E, Chan S P and Reed G T 2006 *Opt. Express* **14** 6469–78
[119] Trinh P D, Yegnanarayanan S, Coppinger F and Jalali B 1997 *IEEE Photon. Technol. Lett.* **9** 940–2
[120] Jia K, Yang J, Hao Y, Jiang X, Wang M, Wang W, Wu Y and Wang Y 2006 *IEEE J. Sel. Top. Quantum Electron.* **12** 1329–34
[121] Qian Y, Kim S, Song J, Nordin G P and Jiang J 2006 *Opt. Express* **14** 6020–8
[122] Wang W, Tang Y, Li T, Wu Y, Yang J and Wang Y 2005 *Appl. Opt.* **44** 2409–15
[123] Lardenois S, Pascal D, Vivien L, Cassan E, Laval S, Orobtchouk R, Heitzmann M, Bouzaida N and Mollard L 2003 *Opt. Lett.* **28** 1150–2
[124] Galli M *et al* 2005 *IEEE J. Sel. Areas Commun.* **23** 1402–10
[125] Settle M, Salib M, Michaeli A and Krauss T F 2006 *Opt. Express* **14** 2440–5
[126] Belotti M, Torres J, Roy E, Pépin A, Gerace D, Andreani L C, Galli M and Chen Y 2006 *Microelectron. Eng.* **83** 1773–7
[127] Little B E, Foresi J S, Steinmeyer G, Thoen E R, Chu S T, Haus H A, Ippen E P, Kimerling L C and Greene W 1998 *IEEE Photon. Technol. Lett.* **10** 549–51
[128] Almeida V R and Lipson M 2004 *Opt. Lett.* **29** 2387–9
[129] Martinez L and Lipson M 2006 *Opt. Express* **14** 6259–63
[130] Lee M C M and Wu M C 2006 *Opt. Express* **14** 4703–12
[131] Indukuri T, Koonath P and Jalali B 2005 *Appl. Phys. Lett.* **87** 081114
[132] Koonath P, Indukuri T and Jalali B 2004 *Appl. Phys. Lett.* **85** 1018–20
[133] Zhou L and Poon A W 2006 *Opt. Express* **14** 6851–7
[134] Kiyat I, Aydinli A and Dagli N 2005 *Opt. Express* **16** 1900–5
[135] Xia F, Sekaric L and Vlasov Y A 2006 *Opt. Express* **14** 3872–86
[136] Timotijevic B D, Gardes F Y, Headley W R, Reed G T, Paniccia M J, Cohen O, Hak D and Masanovic G Z 2006 *J. Opt. A: Pure Appl. Opt.* **8** S473-6
[137] Ta'eed V G, Moss D J, Eggleton B J, Freeman D, Madden S, Samoc M, Luther-Davies B, Janz S and Xu D X 2004 *Opt. Express* **12** 5274–84
[138] Vivien L, Roux X L, Laval S, Cassan E and Marris-Morini D 2006 *IEEE J. Sel. Top. Quantum Electron.* **12** 1354–8
[139] Harke A, Krause M and Mueller J 2005 *Electron. Lett.* **41** 1377–9
[140] Grillot F, Vivien L, Laval S and Cassan E 2006 *J. Lightwave Technol.* **24** 891–6
[141] Tien P K 1971 *Appl. Opt.* **10** 2395–413
[142] Lee K K, Lim D R, Luan H C, Agrawal A, Foresi J and Kimerling L C 2000 *Appl. Phys. Lett.* **77** 1617–9
[143] Marcuse D 1969 *Bell Syst. Tech. J.* **48** 3187–215
[144] Payne F P and Lacey J P R 1994 *Opt. Quantum Electron.* **26** 977–86
[145] Vlasov Y A and McNab S J 2004 *Opt. Express* **12** 1622–31
[146] Lee K K, Lim D R, Kimerling L C, Shin J and Cerrina F 2001 *Opt. Lett.* **26** 1888–90
[147] Sparacin D K, Spector S J and Kimerling L C 2005 *J. Lightwave Technol.* **23** 2455–61
[148] Lee M C M and Wu M C 2006 *J. Microelectromech. Syst.* **15** 338–43
[149] Borselli M, Johnson T J and Painter O 2005 *Opt. Express* **13** 1515–30
[150] Dimitropoulos D, Jhaveri R, Claps R, Woo J C S and Jalali B 2005 *Appl. Phys. Lett.* **86** 071115
[151] Sze S M 1981 *Physics of Semiconductor Devices* (Wiley: New York)
[152] Liu Y and Tsang H K 2006 *Opt. Lett.* **31** 1714–16
[153] Lui K P H and Hegmann F A 2003 *J. Appl. Phys.* **93** 9012–8
[154] Knights A P and Hopper G F 2003 *Electron. Lett.* **39** 1036
[155] OlympIOs, http://www.c2v.nl
[156] Nguyen V, Montalbo T, Manolatou C, Agarwal A, Hong C, Yasaitis J, Kimerling L C and Michel J 2006 *Appl. Phys. Lett.* **88** 081112
[157] Delâge A, Janz S, Lamontagne B, Bogdanov A, Dalacu D, Xu D X and Yap K P 2006 *Opt. Express* **14** 148–61
[158] Aalto T, Solehmainen K, Harjanne M, Kapulainen M and Heimala P 2006 *IEEE Photon. Technol. Lett.* **18** 709–11
[159] Almeida V R, Panepucci R R and Lipson M 2003 *Opt. Lett.* **28** 1302–4
[160] Shoji T, Tsuchizawa T, Watanabe T, Yamada K and Morita H 2002 *Electron. Lett.* **38** 1669–70
[161] Choudhury A N M M, Stanczyk T R, Richardson D, Donval A, Oron R and Oron M 2005 *IEEE Photon. Technol. Lett.* **17** 1881–3
[162] Dai D, He S and Tsang H K 2006 *J. Lightwave Technol.* **24** 2428–33

[163] Lamontagne B, Cheben P, Post E, Janz S, Xu D X and Delâge A 2006 *J. Vac. Sci. Technol.* A **24** 718–22
[164] Wang B, Jiang J and Nordin G P 2005 *IEEE Photon. Technol. Lett.* **17** 1884–6
[165] Taillaert D, Bienstman P and Baets R 2004 *Opt. Lett.* **29** 2749–51
[166] Orobtchouk R, Layadi A, Gualous H, Pascal D, Koster A and Laval S 2000 *Appl. Opt.* **39** 5773–7
[167] Masanovic G Z, Reed G T, Headley W, Timotijevic B, Passaro V M N, Atta R, Esnell G and Evans A G R 2005 *Opt. Express* **13** 7374–9
[168] Luyssaert B, Vandersteegen P, Tailleart D, Dumon P, Bogaerts W, Bienstman P, Thourhout D V, Wiaux V, Beckx S and Baets R 2005 *IEEE Photon. Technol. Lett.* **17** 73–5
[169] Chen H T and Web K J 2006 *Opt. Lett.* **31** 2145–7
[170] Bachelot R, Fares A, Fikri R, Barchiesi D, Lerondel G and Royer P 2004 *Opt. Lett.* **29** 1–3
[171] Agrawal G P 2002 *Fiber-Optic Communications Systems* 3rd edn (New York: Wiley)
[172] Dulkeith E, Xia F, Schares L, Green W M J and Vlasov Y A 2006 *Opt. Express* **14** 3853–63
[173] TSang H K, Wong C S, Liang T K, Day I E, Roberts S W, Harpin A, Drake J and Asghari M 2002 *Appl. Phys. Lett.* **80** 416–8
[174] FieldDesigner, http://www.phoenixbv.com
[175] Palik E D 1998 *Handbook of Optical Constants of Solids* (New York: Academic)
[176] Yu P Y and Cardona M 2005 *Fundamentals of Semiconductors: Physics and Material Properties*, 3rd edn (Berlin: Springer)
[177] Yin L, Lin Q and Agrawal G P 2006 *Opt. Lett.* **31** 1295–7
[178] Turner A C, Manolatou C, Schmidt B S, Lipson M, Foster M A, Sharping J E and Gaeta A L 2006 *Opt. Express* **14** 4357–62
[179] Lou J, Tong L and Ye Z 2006 *Opt. Express* **14** 6993–8
[180] Dimitropolous D, Raghunathan V, Claps R and Jalali B 2003 *Opt. Express* **12** 149–60
[181] Chan S P, Passaro V M N and Reed G T 2005 *Electron. Lett.* **41** 528–9
[182] Headley W R, Reed G T, Howe S, Liu A and Paniccia M 2004 *Appl. Phys. Lett.* **85** 5523–5
[183] Krause M, Renner H and Brinkmeyer E 2006 *IEEE J. Sel. Top. Quantum Electron.* **12** 1359–1362
[184] Reed G T *et al* 2006 *IEEE J. Sel. Top. Quantum Electron.* **12** 1335–44
[185] Ye W N, Xu D X, Janz S, Cheben P, Picard M J, Lamontagne B and Tarr N G 2005 *J. Lightwave Technol.* **23** 1308–18
[186] Xu D X, Janz S and Cheben P 2006 *IEEE Photon. Technol. Lett.* **18** 343–5
[187] Chen C H, Pang L, Tsai C H, Levy U and Fainman Y 2005 *Opt. Express* **13** 5347–52
[188] Kakihara K, Kono N, Saitoh K, Fujisawa T and Koshiba M 2006 *Opt. Express* **14** 7046–56
[189] Brooks C, Jessop P E, Deng H, Yevick D O and Tarr G 2006 *Opt. Eng.* **45** 044603
[190] Deng H, Yevick D O, Brooks C and Jessop P E 2005 *J. Lightwave Technol.* **23** 432–45
[191] Soref R A, Schmidtchen J and Petermann K 1971 *IEEE J. Quantum Electon.* **27** 1971–4
[192] Lousteau J, Furniss D, Seddon A B, Benson T M, Vukovic A and Sewell P 2004 *J. Lightwave Technol.* **22** 1923–9
[193] Powell O 2002 *J. Lightwave Technol.* **20** 1851–5
[194] Xia J and Yu J 2004 *Opt. Commun.* **230** 253–7
[195] Chan S P, Png C E, Lim S T, Reed G T and Passaro V M N 2005 *J. Lightwave Technol.* **23** 2103–11
[196] Tong L, Lou J and Mazur E 2004 *Opt. Express* **12** 1025–35
[197] Fujisawa T and Koshiba M 2006 *IEEE Photon. Technol. Lett.* **18** 1530–2
[198] Xu Q, Almeida V R, Panepucci R R and Lipson M 2004 *Opt. Lett.* **29** 1626–8
[199] Anderson P A, Schmidt B S and Lipson M 2006 *Opt. Express* **14** 9197–202
[200] Baehr-Jones T, Hochberg M, Walker C and Scherer A 2005 *Appl. Phys. Lett.* **86** 081101
[201] Barrios C A 2004 *Electron. Lett.* **40** 862–3
[202] Fujisawa T and Koshiba M 2006 *Opt. Lett.* **31** 56–8